

DTIC FILE COPY



# NAVAL POSTGRADUATE SCHOOL Monterey, California

AD-A230 855



DTIC  
ELECTE  
JAN 29 1991  
S B D

## THESIS

SURFACE DYNAMICS OF UNIPOLAR ARCING

by

Richard Keith Downs

December 1989

Thesis Advisor

Fred R. Schwirzke

Approved for public release; distribution is unlimited.

01 1 28 091

Unclassified

security classification of this page

REPORT DOCUMENTATION PAGE

1a Report Security Classification <b>Unclassified</b>		1b Restrictive Markings	
2a Security Classification Authority		3 Distribution Availability of Report	
2b Declassification Downgrading Schedule		Approved for public release; distribution is unlimited.	
4 Performing Organization Report Number(s)		5 Monitoring Organization Report Number(s)	
6a Name of Performing Organization Naval Postgraduate School	6b Office Symbol (if applicable) 33	7a Name of Monitoring Organization Naval Postgraduate School	
6c Address (city, state, and ZIP code) Monterey, CA 93943-5000		7b Address (city, state, and ZIP code) Monterey, CA 93943-5000	
8a Name of Funding Sponsoring Organization	8b Office Symbol (if applicable)	9 Procurement Instrument Identification Number	
8c Address (city, state, and ZIP code)		10 Source of Funding Numbers	
		Program Element No	Project No
		Task No	Work Unit Accession No
11 Title (include security classification) <b>SURFACE DYNAMICS OF UNIPOLAR ARCING</b>			
12 Personal Author(s) <b>Richard Keith Downs</b>			
13a Type of Report Master's Thesis	13b Time Covered From To	14 Date of Report (year, month, day) December 1989	15 Page Count 101
16 Supplementary Notation The views expressed in this thesis are those of the author and do not reflect the official policy or position of the Department of Defense or the U.S. Government.			
17 Cosati Codes		18 Subject Terms (continue on reverse if necessary and identify by block number)	
Field	Group	Subgroup	unipolar arcing, surface, surface tension, arc welding, laser, laser-target-interaction, plasma. ↑
1		2	
19 Abstract (continue on reverse if necessary and identify by block number)			
<p>A 4.55 microsecond, 15 Joule pulsed CO2 laser was used to illuminate a copper target. Bulk plasma was found to be emitted normally to the target surface independent of the laser angle of incidence over the range of <math>45^\circ \pm 15^\circ</math>. Material ejected from a copper target was allowed to deposit onto polished type 304 stainless steel surfaces. The ejected material deposited in concentric 'rings' in many places. The mechanism for this is unknown.</p> <p>Polished type 304 stainless steel surfaces were coated with one to ten micron copper films and shot with the laser. Damage to the films indicate that the damage mechanism may simply be joule heating from the arc current. This lead to a procedure for calculating that arc current. The arc lifetime is necessary but still unknown. No correlation was found between unipolar arc pit diameter and depth.</p> <p>Investigations into the role of surface tension on the dynamics of the molten surface lead to a comparison between unipolar arcing and arc welding. Much of the physics known about arc welding is qualitatively applied to describe the surface dynamics of molten metal produced by unipolar arcing.</p>			
20 Distribution Availability of Abstract		21 Abstract Security Classification	
<input checked="" type="checkbox"/> unclassified unlimited <input type="checkbox"/> same as report <input type="checkbox"/> DTIC users		Unclassified	
22a Name of Responsible Individual Fred R. Schwirzke		22b Telephone (include Area code) (408) 646-2635	22c Office Symbol 61Sw

Approved for public release; distribution is unlimited.

Surface Dynamics of Unipolar Arcing

by

Richard Keith Downs  
Lieutenant, United States Navy  
B.S., University of Texas-Austin, 1981

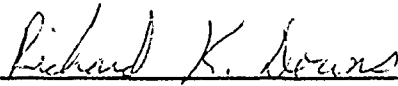
Submitted in partial fulfillment of the  
requirements for the degree of

MASTER OF SCIENCE IN PHYSICS

from the

NAVAL POSTGRADUATE SCHOOL  
December 1989

Author:

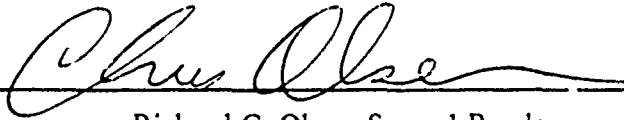


Richard Keith Downs

Approved by:



Fred R. Schwirzke, Thesis Advisor



Richard C. Olsen, Second Reader



Karlheinz E. Woehler, Chairman,  
Department of Physics

## ABSTRACT

A 4.55 microsecond, 15 Joule pulsed CO<sub>2</sub> laser was used to illuminate a copper target. Bulk plasma was found to be emitted normally to the target surface independent of the laser angle of incidence over the range of  $45^\circ \pm 15^\circ$ . Material ejected from a copper target was allowed to deposit onto polished type 304 stainless steel surfaces. The ejected material deposited in concentric 'rings' in many places. The mechanism for this is unknown.

Polished type 304 stainless steel surfaces were coated with one to ten micron copper films and shot with the laser. Damage to the films indicate that the damage mechanism may simply be joule heating from the arc current. This lead to a procedure for calculating that arc current. The arc lifetime is necessary but still unknown. No correlation was found between unipolar arc pit diameter and depth.

Investigations into the role of surface tension on the dynamics of the molten surface lead to a comparison between unipolar arcing and arc welding. Much of the physics known about arc welding is qualitatively applied to describe the surface dynamics of molten metal produced by unipolar arcing.

<b>Accession For</b>	
NTIS GRA&I	<input checked="" type="checkbox"/>
DTIC TAB	<input type="checkbox"/>
Unannounced	<input type="checkbox"/>
Justification	
By _____	
Distribution/	
Availability Codes	
Dist	Avail and/or Special
A-1	



## TABLE OF CONTENTS

I. INTRODUCTION .....	1
II. BACKGROUND AND THEORY .....	3
A. BACKGROUND .....	3
1. Definition of a plasma .....	3
2. Debye shielding .....	4
3. Plasma generation by the CO <sub>2</sub> laser .....	5
B. THE ROBSON-THONEMAN MODEL .....	7
C. THE SCHWIRZKE MODEL .....	10
D. THIN FILMS .....	11
E. THIN FILMS AND THE UNIPOLAR ARC .....	15
III. EQUIPMENT AND PROCEDURES .....	17
A. EQUIPMENT .....	17
1. Vapor Deposition System .....	17
a. Sander and Polishing Wheels .....	17
b. Ultrasonic Cleaning System .....	17
c. Pure-Air System .....	17
d. Vapor Degreaser .....	18
e. VEECO VE-401 Automatic High Vacuum Evaporator .....	18
f. Deposit Thickness Monitor .....	20
2. CO <sub>2</sub> Laser System .....	21
a. CO <sub>2</sub> Laser .....	21
b. Target Chamber .....	21
c. Energy Meter and Probe .....	22
d. Optics .....	23
3. Analysis Equipment .....	24
a. Optical Microscope .....	24
b. Scanning Electron Microscope .....	24
B. THE EXPERIMENTAL PROCEDURE .....	25
1. Calibration .....	25

2. Target Preparation .....	28
IV. EXPERIMENTAL RESULTS AND DISCUSSION .....	31
A. INITIAL INVESTIGATIONS .....	31
1. Normal Emission of Bulk Material .....	31
2. Deposition profile of ejected bulk material .....	33
B. THIN FILMS AND THE UNIPOLAR ARC .....	42
1. Arc damage - a heating phenomenon .....	42
2. Calculation of Unipolar Arc Current .....	43
3. Pit depth experiment .....	49
V. THE SURFACE DYNAMICS OF UNIPOLAR ARCING .....	56
A. PIT FORMATION .....	56
1. Forces which tend to open a pit .....	56
2. Forces which tend to close a pit .....	59
3. Overview of the dynamics of pit formation .....	60
B. RIM FORMATION .....	61
1. Dynamics due to the ejected vapor .....	61
2. Dynamics due to surface tension .....	64
a. Full film penetration .....	64
b. Flow induced by a surface tension gradient .....	65
VI. CONCLUSIONS .....	74
APPENDIX A. RAW DATA FROM PIT DEPTH VERSUS DIAMETER EX- PERIMENTS .....	76
APPENDIX B. ION ENERGY CONTRIBUTION .....	78
A. RECOMBINATION ENERGY CONTRIBUTION .....	78
B. KINETIC ENERGY CONTRIBUTION .....	79
APPENDIX C. DETAILED CALCULATION OF THE SHEAR STRESS .....	82
LIST OF REFERENCES .....	85

INITIAL DISTRIBUTION LIST ..... 88

## LIST OF TABLES

Table 1.	DATA FOR SHOTS A THROUGH D. ....	38
Table 2.	DATA FOR PITS WHICH DID NOT PENETRATE THE COPPER FILM. ....	76
Table 3.	DATA FOR PITS WHICH PENETRATED THE COPPER FILM. ...	77

## LIST OF FIGURES

Figure 1.	Equilibrium Plasma-Surface Interaction Prior to Cathode Spot Formation.	8
Figure 2.	Plasma-Surface Interaction During Unipolar Arcing. ....	9
Figure 3.	Local Electric Field Enhancement at a Whisker Tip. ....	11
Figure 4.	Schwirzke Unipolar Arc Model. ....	12
Figure 5.	Oval Dimple Boat. ....	13
Figure 6.	Oval Dimple Boat Evaporation Distribution Profiles. ....	14
Figure 7.	3/8 inch I.D. X 6 Coil. ....	14
Figure 8.	Coil Evaporation Distribution Profiles. ....	15
Figure 9.	Ultrasonic System ....	18
Figure 10.	VE-401 Automatic High Vacuum Evaporator. ....	19
Figure 11.	Lumonics TE-822HP CO <sub>2</sub> Laser ....	22
Figure 12.	Target Chamber. ....	23
Figure 13.	ZEISS ICM 405 Inverted Camera Microscope ....	24
Figure 14.	Basic Schematic Diagram of the Operation of the SEM. ....	26
Figure 15.	500X Photograph of the DTM Crystal's Edge after Deposition. ....	27
Figure 16.	Equipment Configuration for the Laser Shot. ....	30
Figure 17.	Diagram of first experiment to determine the directionality of material emission from a copper target. ....	32
Figure 18.	Diagram of second experiment to determine the directional dependence of material emission from a copper target. ....	32
Figure 19.	Steel surface showing bulk copper deposition. ....	34
Figure 20.	Copper deposition on a steel surface showing a correlation between greater pitting density with greater copper deposition. ....	34
Figure 21.	Ring structure ....	35
Figure 22.	Second ring structure ....	35
Figure 23.	Circular copper deposits ....	36
Figure 24.	Interference deposition pattern ....	36
Figure 25.	Second interference deposition pattern ....	37
Figure 26.	The region shown in Figure 25 at 500X. ....	37
Figure 27.	Shot A ....	39
Figure 28.	Shot A ....	39

Figure 29. Shot B .....	40
Figure 30. Shot C .....	40
Figure 31. Shot C .....	41
Figure 32. Shot C .....	41
Figure 33. Shot D .....	42
Figure 34. Optical microscope image of a focused laser spot .....	43
Figure 35. SEM image of laser spot. ....	44
Figure 36. Distribution of iron in Figure 35. ....	44
Figure 37. Distribution of copper in Figure 35. ....	45
Figure 38. Optical microscope image of damage outside the laser spot .....	45
Figure 39. Optical microscope image of further damage outside the laser spot ....	46
Figure 40. Calculation data .....	49
Figure 41. Example pit which fully penetrated the copper film. ....	51
Figure 42. Iron distribution of Figure 41. ....	51
Figure 43. Copper distribution of Figure 41. ....	52
Figure 44. Example pit which does not penetrate the copper film. ....	52
Figure 45. Iron distribution in Figure 44. ....	53
Figure 46. Results of pit depth versus pit diameter experiment. ....	54
Figure 47. Example of Unipolar Arc pit diversity. ....	55
Figure 48. Example of Unipolar Arc pit diversity. ....	55
Figure 49. Forces involved in the formation of the pit. ....	57
Figure 50. Vapor pressure versus temperature for Aluminum, Copper and Iron. ..	59
Figure 51. Surface tension coefficient versus temperature for copper. ....	61
Figure 52. Example pit profiles. ....	62
Figure 53. Unipolar arc craters on stainless steel target .....	63
Figure 54. Unipolar arc craters on stainless steel target .....	63
Figure 55. Pit fully penetrating a film over a surface. ....	65
Figure 56. Surface tension forces on a liquid drop in contact with a surface. ....	66
Figure 57. The current $I$ enters at the origin of the coordinate system and flows radially into a conducting fluid. ....	67
Figure 58. Effect on the surface tension of iron by various non- metallic elements. 71	71
Figure 59. Effect on the surface tension of copper by oxygen and sulphur. ....	71
Figure 60. The velocity distribution, streamlines and isotherms .....	72
Figure 61. The velocity distribution, streamlines and isotherms .....	73

Figure 62. Sign convention for flow in terms of a change in the stream function. . . 73

Figure 63. Components of viscous in the spherical coordinate system. . . . . 83

## ACKNOWLEDGEMENTS

I want to take this opportunity to thank some people who were of great help in researching this thesis. I thank Robert Sanders and Don Spiel for teaching me to operate the equipment correctly, thanks to George Jaksha and Steve Blankschein for their making the tools I needed, and Tom Kellogg for taking time out of his busy schedule to operate the scanning electron microscope. Most of all. I thank Maria T. Woznyj, my fiancee, for her unwavering support and faith in me as I pursued this research.

## I. INTRODUCTION

In the search for an almost infinite and clean energy source mankind has looked towards nuclear fusion. In this endeavor the understanding of the properties of plasmas is a necessary undertaking. Since we are unable to produce machines of infinite size, we must pay particular attention to the interactions between the plasma and the surfaces of the machines used to contain it.

The plasma-surface interaction occurs primarily through the following erosion processes:

- Sputtering
- Unipolar Arcing
- Heat pulses
- Gases which implant into the surface can generate chemical erosion, embrittlement and blistering.

These processes are of concern due to their limiting the life of equipment components and their resultant introduction of impurities into the plasma. Of these processes it is widely believed that Unipolar Arcing is dominant.

Most research into Unipolar Arcing has thus far investigated only the plasma above the surface. This thesis starts an investigation of the dynamics of the surface itself. It begins with experiments to determine if the bulk emission of material has any directional dependance. The results of these experiments indicate that not only is there directional dependance but there is also more structure to the ejected material than previously thought.

Thin films are used for two purposes: to see how the same arc interacts with two different materials and to find if there is any correlation between pit depth and diameter. It was found that the amount of damage may be dependant upon the material's melting and boiling points. This also lead to a method for calculating the arc current and to the role of surface tension. Investigation into the role of the surface tension lead to the realization of the similarity between Unipolar Arcing and the physics of arc welding. This relationship is exploited in Chapter V which provides a preliminary theory for the surface dynamics. No correlation was found between pit depth and diameter, however these experiments indicate that, for the parameters used, the maximum pit depth is be-

tween 5.5 and 10 microns. In all this research the Unipolar Arcs are generated by a plasma which itself is produced by a CO2 laser.

## II. BACKGROUND AND THEORY

How high energy laser pulses and plasmas interact with various material surfaces has long been under study. Of particular interest has been how laser pulses damage a target surface when the energy of the photons in those pulses is less than the energy necessary for photo-ionization of the material. Presented here is one of the current theories describing this process, it involves the process known as unipolar arcing.

### A. BACKGROUND

Before going into the theories delving into unipolar arcing some background must be given on plasmas and their interactions with surfaces. This section begins with a definition of what a plasma is and mentions some of its properties. The Debye length is derived and a brief description is given on how a plasma is produced by a pulse from a CO<sub>2</sub> laser.

#### 1. Definition of a plasma

In nature there are four states of matter, these are solid, liquid, gas and plasma. These states represent increasing levels of disorder and require higher energy levels with progress from one to the next. The solid is the state of lowest energy and consists of a concentration of atoms or molecules bound together in a rigid lattice structure by their mutual electrical attraction. As energy, heat, is added these atoms will vibrate more and more strongly until they can no longer maintain their lattice structure. In this regime the atoms can move about but their energy is not sufficient to fully overcome their mutual attraction. This is the liquid phase. When more energy is added so that the atoms can completely overcome their mutual electrical attraction they enter the gaseous state. To form a plasma it is necessary to ionize a portion of this gas. That is, sufficient energy must be given to at least one electron in an atom to free it from that atom. This results in a gas composed of both neutral and charged particles. Chen [Ref. 1, p.3] defines a plasma as

A plasma is a quasineutral gas of charged and neutral particles which exhibit collective behavior.

The term 'quasineutral' simply means that the gas contains approximately equal concentrations of ions,  $n_i$ , and electrons,  $n_e$ , such that

$$n_i \approx n_e \approx n \quad \{1\}$$

where  $n$  is called the plasma density. Collective behavior comes from the charged particles. These particles produce and are affected by electric and magnetic fields. Because of this, elements of the plasma will exert forces on one another even at a considerable distance. Thus they will act together, hence the term collective behavior.

Temperature is another property of a plasma. If it is in thermal equilibrium then the temperature is related to the average kinetic energy of its particles by the equation

$$E_{av} = \frac{3}{2} kT. \quad \{2\}$$

Here  $k$  is the Boltzmann constant

$$k = 1.38 \times 10^{-23} \text{ J/K} \quad \{3\}$$

and  $T$  is the absolute temperature in kelvins.

## 2. Debye shielding

Debye shielding refers to the ability of a plasma to shield out electric potentials which are applied to it. When an electric field is applied to a plasma the electrons and ions will drift in opposite directions in response to this field. The charge separation between the electrons and ions acts to counter the applied electric field until it is essentially cancelled out. For instance if a positively charged ball is placed in the plasma it will attract the electrons and repel the ions. The electrons will form a cloud of equal charge around the ball thus effectively cancelling its electric field.

An approximate width of the charge separation caused by a potential,  $\Phi$ , can be easily deduced if all of the motion is considered to be done by the electrons. The fact that the ions are so much more massive than the electrons makes this a good assumption. The ions will then form a uniform background upon which the electron motion takes place. The ion density will be the same locally as it is at a large distance, hence

$$n_i = n_\infty \quad \{4\}$$

Assuming that the potential is held at a fixed value,  $\Phi_0$ , on a plane at  $x=0$ , then  $\Phi(x)$  is desired. Poisson's equation in one dimension is

$$\epsilon_0 \nabla^2 \Phi = \epsilon_0 \frac{d^2 \Phi}{dx^2} = -e(n_i - n_e). \quad \{5\}$$

The Boltzmann relation for the density of electrons is

$$n_e = n_{\infty} e^{\frac{e\Phi}{kT_e}} \quad \{6\}$$

so that equation (5) becomes

$$\epsilon_0 \frac{d^2 \Phi}{dx^2} = en_{\infty} \left[ e^{\frac{e\Phi}{kT_e}} - 1 \right]. \quad \{7\}$$

The solution to this equation is

$$\Phi(x) = \Phi_0 e^{-\frac{|x|}{\lambda_D}} \quad \{8\}$$

where  $\lambda_D$  is the debye length and is defined as

$$\lambda_D \equiv \sqrt{\frac{\epsilon_0 kT_e}{ne^2}}. \quad \{9\}$$

The debye length is a measure of the shielding distance. It is the distance over which the potential is reduced to 1/e of its maximum value.

### 3. Plasma generation by the CO<sub>2</sub> laser

In this research the plasma was generated by a CO<sub>2</sub> laser. The laser sends an electromagnetic pulse to the target. If the target is considered to be at  $x=0$  and the pulse travelling to the left on the x-axis, then the electric field of the incoming laser pulse,  $E_i$ , is given by

$$E_i = E_{oi} \sin\left(\frac{2\pi x}{\lambda} + \omega t\right) \quad \{10\}$$

where  $E_{oi}$  = maximum amplitude of the E-field

$\lambda$  = laser wavelength

$\omega$  = angular frequency

t = time.

For simplicity the target is assumed to be perfectly reflecting. The electric field of the reflected pulse is then

$$E_r = E_{or} \sin\left(\frac{2\pi x}{\lambda} - \omega t + \varepsilon\right) \quad \{12\}$$

where  $\varepsilon$  is a phase angle. Perfect reflection also provides that

$$E_{oi} = E_{or} = E_o. \quad \{13\}$$

If the target is a perfect conductor, then the electric field at  $x=0$  parallel to its surface must be zero. Thus  $\varepsilon = 0$ . The superposition of these waves produces a standing wave whose electric field is given by

$$E = 2E_o \sin\left(\frac{2\pi x}{\lambda}\right) \cos(\omega t) \quad \{14\}$$

and whose intensity is

$$E^2 = 4E_o^2 \sin^2\left(\frac{2\pi x}{\lambda}\right). \quad \{15\}$$

Assuming that an initial electron concentration exists, then electrons above the surface will oscillate in response to this electric field. Maximum oscillations will occur at the maxima of the standing wave, i.e. at  $x = \lambda/4, 3\lambda/4$ , etc.. The source of this initial electron concentration is as yet unclear.

An actual target surface is not perfectly reflecting, thus some of the energy of the laser pulse will be absorbed by that surface. As the target is heated neutral particles adsorbed will be released. Oscillating electrons will collide with these neutrals ionizing many of them. When they are ionized the neutrals release electrons which in turn oscillate and collide producing further ionizations. This process continues until the plasma density rises to a point where the plasma frequency is equal to the laser frequency. The laser will then be reflected by the plasma. The plasma frequency,  $\omega_p$ , is given by

$$\omega_p = \sqrt{\frac{ne^2}{\varepsilon_o m}} \quad \{16\}$$

where  $e$  and  $m$  are the charge and mass of the electron. Thus the plasma density obtained will be

$$n = \frac{\varepsilon_o m \omega_p^2}{e^2} \quad \{17\}$$

which for the CO<sub>2</sub> laser ( $\lambda = 10.6$  micron) yields a critical plasma density of

$$n = 9.93 \times 10^{18} \text{ cm}^{-3}.$$

## B. THE ROBSON-THONEMAN MODEL

In 1958 Robson and Thoneman [Ref. 2] observed what they described to be unipolar arcing occurring on a mercury electrode in the presence of a high energy plasma. Their explanation of this phenomenon follows.

Whenever a metal plate is exposed to a plasma it will collect both the positive ions and the negative electrons. The electrons having much higher random velocities than the ions will initially collect on the plate more rapidly. An electrically isolated metal plate will collect a negative charge and thus a negative potential. This negative potential will repel electrons even as the now more positive potential of the plasma near the surface attracts them. Only the electrons at the high end of their maxwellian distribution will have sufficient energy to overcome these potentials and reach the plate. At equilibrium this potential is known as the floating potential (Figure 1).

The negatively charged plate receives an ion current density of

$$j_i = n_i e_i v_i \quad \{19\}$$

where  $n_i$  = ion density

$e_i$  = ion charge

$v_i$  = mean velocity with which the ions reach the sheath boundry

$$= \alpha \sqrt{\left( \frac{k T_e}{M} \right)}$$

$M$  = ion mass

$T_e$  = electron temperature

$\alpha$  = factor on the order of unity.

Given that the plate potential with respect to the plasma is  $V$ , then the electron current density is

$$j_e = \frac{1}{4} n_e e_e v_e e^{-\frac{e_e V}{k T_e}} \quad \{21\}$$

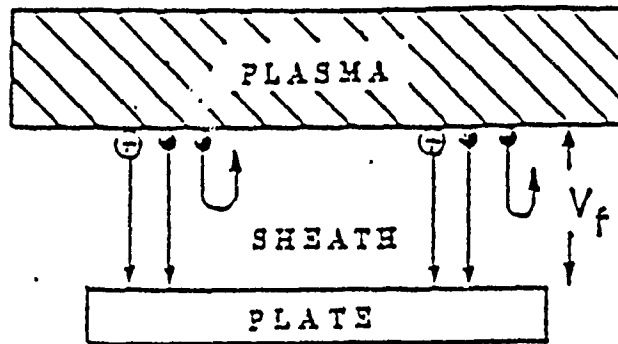


Figure 1. Equilibrium Plasma-Surface Interaction Prior to Cathode Spot Formation.

where  $n_e$  = electron density

$e_e$  = electron charge

$v_e$  = mean random velocity of the plasma electrons

$$= \sqrt{\frac{8kT_e}{\pi m}}$$

$m$  = electron mass.

In steady state the plate is at the floating potential,  $V_f$ , and the total current is

$$j_i + j_e = 0. \quad \{23\}$$

Assuming that  $\alpha \approx 1$  and  $e_i = -e_e$  (i.e. singly charged ions) then we have

$$\begin{aligned} j_i &= -j_e \\ n_i e_i \alpha \sqrt{\frac{kT_e}{M}} &= -\frac{1}{4} n_e e_e \sqrt{\frac{8kT_e}{\pi m}} e^{-\frac{e_e V_f}{kT_e}} \\ \sqrt{\frac{1}{M}} &= \sqrt{\frac{1}{2\pi m}} e^{-\frac{e_e V_f}{kT_e}} \\ \frac{e_e V_f}{e kT_e} &= \sqrt{\frac{M}{2\pi m}} \\ V_f &= \frac{kT_e}{2e_e} \ln\left(\frac{M}{2\pi m}\right). \end{aligned} \quad \{24\}$$

This equation shows that given a sufficiently high electron temperature,  $T_e$ , the floating potential,  $V_f$ , will surpass that needed to sustain an arc. Such an arc current of electrons from the plate to the plasma will lower the local potential between the plate and plasma to the cathode fall potential of the arc,  $V_c$ . This lower potential will allow more electrons from the high energy end of their maxwellian distribution to cross the sheath from the plasma to the plate thus completing the circuit (Figure 2). There is then a circulating current which maintains the requirement that the total current to the plate be zero. The circulating current is described by

$$I_c = A n e_e \sqrt{\frac{kT_e}{2\pi m}} \left\{ e^{-\frac{e_e V_c}{kT_e}} - e^{-\frac{e_e V_f}{kT_e}} \right\} \quad \{25\}$$

where  $A$  = plate area exposed to the plasma. Thus this is indeed a unipolar arc, an arc which requires only one electrode and runs off the thermal energy of the plasma electrons.

Robson and Thoneman tested their theory by creating a plasma in a vacuum tube and then heating it with RF energy. In their experiments they found good evidence in support of their theory and observed unipolar arcing taking place.

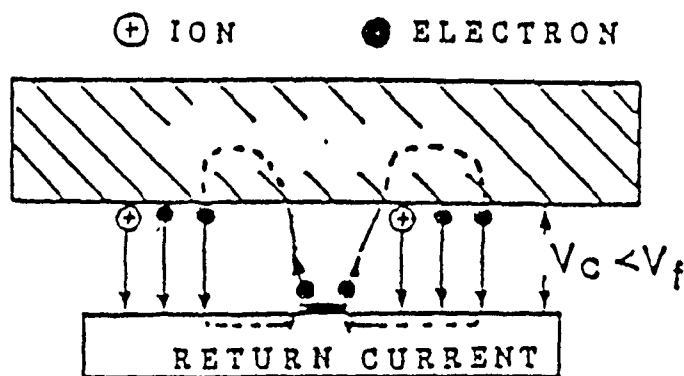


Figure 2. Plasma-Surface Interaction During Unipolar Arcing.

### C. THE SCHWIRZKE MODEL

In 1980 Schwirzke [Ref. 3] expanded upon the Robson-Thoneman model, he connected the unipolar arc phenomenon with the laser-target interaction. A Q-switched neodymium laser was used in his experiments. Later research by Schwirzke found general applicability to Tokamaks [Ref. 4] and the CO2 TEA laser. A plasma in contact with a surface will form a sheath with the floating potential given by

$$V_f = \frac{kT_e}{2e} \ln\left(\frac{M}{2\pi m}\right). \quad \{26\}$$

It was also stipulated that the sheath width is proportional to the Debye length

$$\lambda_D = \sqrt{\frac{kT_e}{4\pi n e^2}}. \quad \{27\}$$

Thus the electric field across this sheath and in a direction normal to the surface will be given by

$$|E_n| \approx \frac{V_f}{\lambda_D} = \sqrt{\pi n k T_e} \ln\left(\frac{M}{2\pi m}\right). \quad \{28\}$$

Unipolar arcing develops if the sheath potential is high enough to sustain an arc. The electric field is then intense enough to cause the emission of electrons from a surface spot into the plasma. "The minimum requirement for the onset of arcing is that the sheath potential is comparable to the ionization energy ..." [Ref. 3] of the material.

"For an arc to develop it is also necessary that the ion density increases in front of the cathode spot in order that a larger electron current can flow into the plasma." [Ref. 3] This occurs when the electric field concentrates around protrusions or 'whiskers' (Figure 3) causing increased ion bombardment and hence heating. The increased local heating causes increased desorption of surface gases, oils and metal evaporation. This causes an increased concentration of neutrals in the sheath of which a small percentage is ionized. The small percentage of ionized neutrals causes a drastic increase in the local ion concentration. These new ions are then accelerated by the sheath potential back to the surface causing further increases in surface temperature, vaporization and electron emission from the hot cathode spot is the result. The locally increased ion concentration above the cathode spot leads to a radial electric field (Figure 4) given by

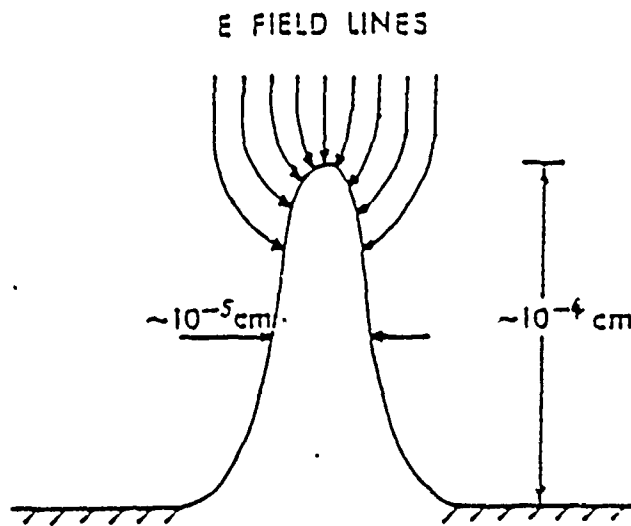


Figure 3. Local Electric Field Enhancement at a Whisker Tip.

$$E_r = - \left( \frac{kT_e}{e} \right) \left( \frac{1}{n} \right) \left( \frac{dn}{dr} \right). \quad \{29\}$$

"This reduces the potential in a ring-like area surrounding the higher pressure region above the arc spot. The sheath potential will be lowered there and more electrons from the high energy tail of the Maxwellian distribution can reach the surface, thus closing the current loop." [Ref. 3]

#### D. THIN FILMS

Thin films [Ref. 5] have been prepared for quite a long time. Thin film technology generally refers to the deposition of layers by an atom by atom process as opposed to layers formed by laying down relatively large particles. One of the most important aims in making a thin film is generating continuous layers, large particles may or may not react together to form such layers. The basic techniques for the deposition of thin films are:

- Electroplating
- Chemical Reduction
- Vacuum Evaporation
- Sputtering

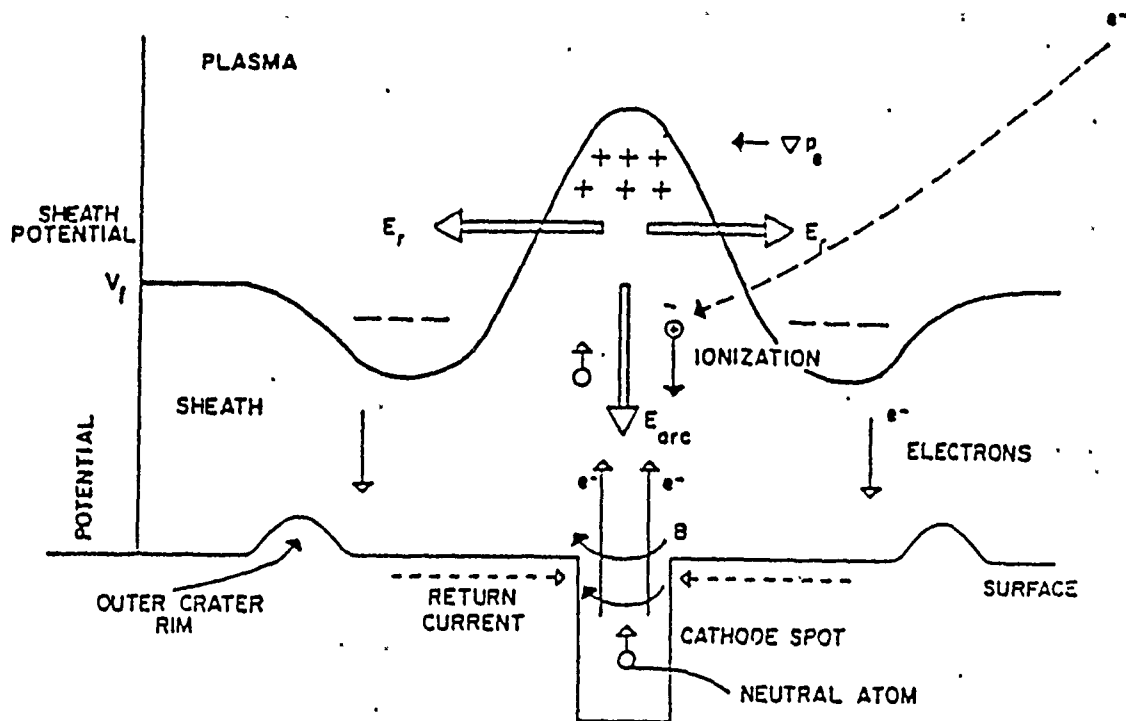


Figure 4. Schwirzke Unipolar Arc Model.

- Chemical Vapor Deposition

In the research reported in this thesis the vacuum evaporation method was used. The method of thin film production by evaporation consists of four physical stages:

- conversion of the material to be deposited into a gaseous state;
- transport to the substrate;
- deposition onto the substrate;
- rearrangement or modifications of their binding as more material arrives.[Ref. 6]

Vacuum evaporation requires a relatively clean vacuum in a range typically obtained by a modern ion or diffusion pump system. In this vacuum a vapor source will develop a rate of vaporization given by

$$N_e = 3.513 \times 10^{22} \frac{a_i P_e}{\sqrt{M_e T}} \frac{\text{molecules}}{\text{cm}^2 \text{sec}} \quad (30)$$

Where  $a_i$  = evaporation coefficient ( $\approx 1$  for a clean evaporant source)

$M_e$  = element atomic weight of the vapor source

$P_e$  = vapor pressure of the vapor source

$T$  = temperature.

How this vapor finally deposits onto the desired substrate is dependent upon the geometry of the system, that is, it depends upon the geometry of the vapor source, the substrate, and relative positions of the two. For example, using the oval dimple boat in Figure 5 will give deposition profiles given in Figure 6, whereas using the coil in Figure 7 will give the deposition profiles shown in Figure 8 [Ref. 7].

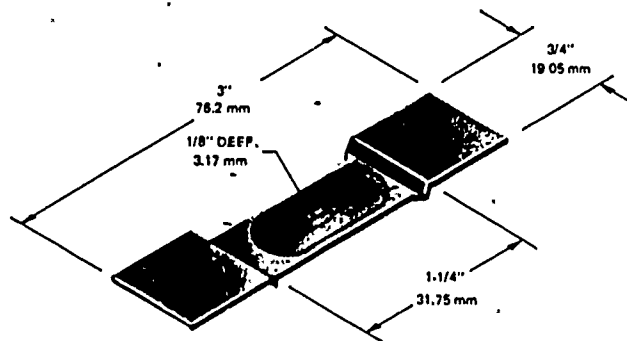


Figure 5. Oval Dimple Boat. [Ref. 7, p.27]

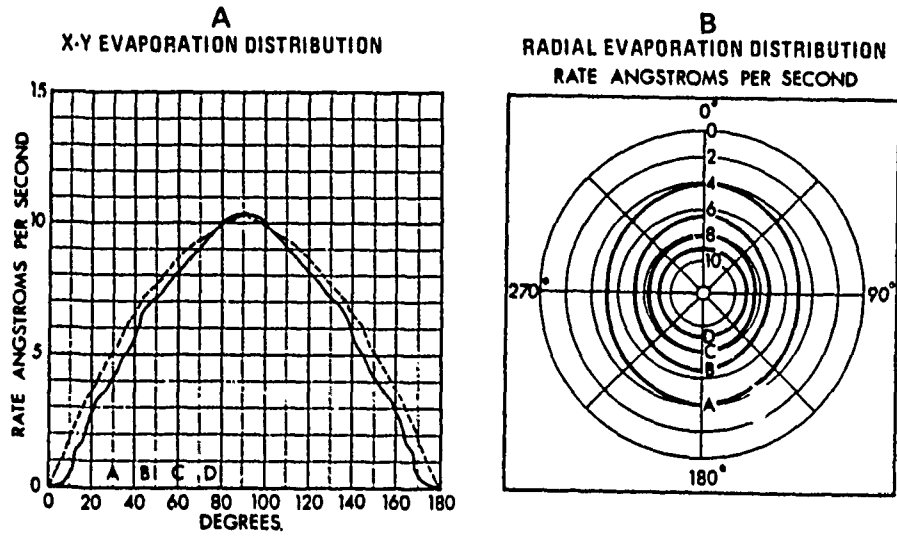


Figure 6. Oval Dimple Boat Evaporation Distribution Profiles. [Ref. 7, p.27]

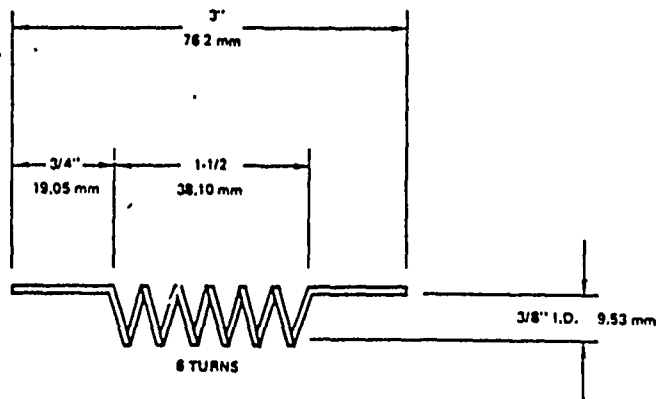


Figure 7. 3/8 inch I.D. X 6 Coil. [Ref. 7, p.110]

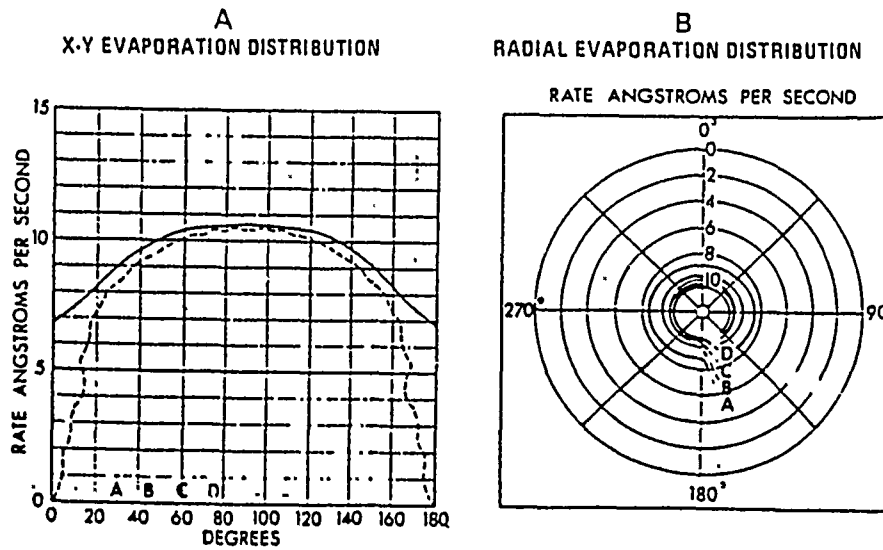


Figure 8. Coil Evaporation Distribution Profiles. [Ref. 7, p.110]

### E. THIN FILMS AND THE UNIPOLAR ARC

The purpose of this thesis is to investigate the dynamics of damage on the surface caused by unipolar arcing. By gaining an understanding of these dynamics methods of preventing damage may be sought after.

This being the first investigation dealing exclusively with the dynamics of the surface, as opposed to the plasma over the surface, the experiments begin simply. While the shape of the pit in the surface is as yet unknown, they appear to tunnel normal to the surface. If the majority of them are indeed normal to the surface, then the gases they eject will be ejected normally. This will occur regardless of the incident angle of the CO<sub>2</sub> laser pulse. The first set of experiments provide a preliminary investigation of this.

How are different materials affected by unipolar arcing? One method is to illuminate different materials with the laser. While this will provide much data on the general differences in their interactions, a more interesting experiment is how the same arc affects two different materials. This the basis of the second set of experiments. In these experiments a thin film of one material, copper, is placed over another, type 304 stainless steel. This actually serves two purposes. The first is to observe differences in damage between the two materials. While it is expected that the film will suffer more damage, just how much more damage is the question. The second purpose is to find an estimate

of the amount of heat generated during the arcing process. Where damage is restricted to the film only, then knowing the material damaged and its volume allows calculation of the heat input. Assuming this heat is provided by the arc current allows its calculation.

Several assumptions have been made in these experiments. Most have been interspersed throughout this report and will be brought up as they are needed. The two most fundamental assumptions are:

- the thin films made are of uniform thickness;
- the boundary between the different materials does not significantly affect the arcing.

Another of the unknowns involved in the study of the unipolar arc phenomenon is the depth of the unipolar arc pits. Knowing the depth of these pits will allow measurement of the actual amount of material ejected from the pit into the surrounding vacuum and may shed further light onto the internal dynamics of the process of the pit formation. The final experiment attempts to determine a relationship between the diameter of the unipolar arc pits and their depth. This is accomplished using thin films of varying thicknesses on a surface which is hit by a high power pulse from a CO<sub>2</sub> laser. These targets are then analyzed to determine the smallest diameter pits which penetrate through to the substrate for each film thickness. This data is then to be used to determine a relationship between the size (diameter) of the pits and their depth.

### III. EQUIPMENT AND PROCEDURES

This research was designed to study the surface dynamics of the molten metal produced by unipolar arcing and to find if there is a relationship between the diameter of the unipolar arc pits and their depth. The equipment used and procedures followed to accomplish this objective are described in the following sections.

#### A. EQUIPMENT

The equipment used in the conduct of the research described in this thesis can be broken down into three categories: the Vapor Deposition System, the CO<sub>2</sub> Laser System, and the analysis equipment. The Vapor Deposition System includes all of the equipment used to prepare the target: sander, polishing wheels, ultrasonic cleaner, pure-air system, vapor degreaser, deposit thickness monitor, and the VEECO VE-401 automatic high vacuum evaporator. The CO<sub>2</sub> laser system includes all of the equipment necessary to impinge a laser pulse onto the target: CO<sub>2</sub> laser, target chamber, energy meter, and the optics. The analysis equipment includes all of the equipment used to analyze the results: optical microscope, and the scanning electron microscope.

##### 1. Vapor Deposition System

The vapor deposition system consists of the equipment used to prepare the target. The equipments used to polish the target are the sander and polishing wheels. The equipment used to clean the target were the ultrasonic cleaner, the pure-air system, and the vapor degreaser. The film deposition was conducted using the VEECO VE-401 automatic high vacuum evaporator and the deposit thickness monitor.

###### *a. Sander and Polishing Wheels*

To produce a smooth surface for film deposition the target underwent a standard polishing procedure using 240, 320, 400 and 600 grit sandpaper. This was followed by further polishing using the standard Buehler polisher with 1.0 micron and 0.05 micron Alumina (a powder suspended in an aqueous solution).

###### *b. Ultrasonic Cleaning System*

The Sonicor ultrasonic system (model SC-101TH) shown in Figure 9 was used to clean all of the targets.

###### *c. Pure-Air System*

In order to clean all particulates and dust off of the surface of the targets a clean environment is necessary. This clean environment was produced by the Model



Figure 9. Ultrasonic System

TM-48 pure air system made by the Pure Air Corporation. This system filters out all 0.5 micron and larger particles and then blows the clean air into a small work area (60 cm deep X 57 cm high X 117 cm wide).

*d. Vapor Degreaser*

This device consisted of a 1000 milliliter beaker, a target holder, a petri dish and a hot plate. A mixture of acetone and ethyl alcohol is added and allowed to boil, the distilled vapors then condense on the target surface and run off by gravity.

*e. VEECO VE-401 Automatic High Vacuum Evaporator*

The VEECO VE-401 automatic high vacuum evaporator [Ref. 8] is shown in Figure 10. It consists of a vacuum system, pressure gauge controls and evaporator equipment. The vacuum system is composed of

- mechanical pump capable of reducing the system pressure to approximately 10 microns;
- diffusion pump capable of lowering the system pressure to the vicinity of  $10^{-7}$  torr;
- cold trap utilizing liquid nitrogen to remove condensable gases and prevent oil vapor from the diffusion pump from entering the bell jar.

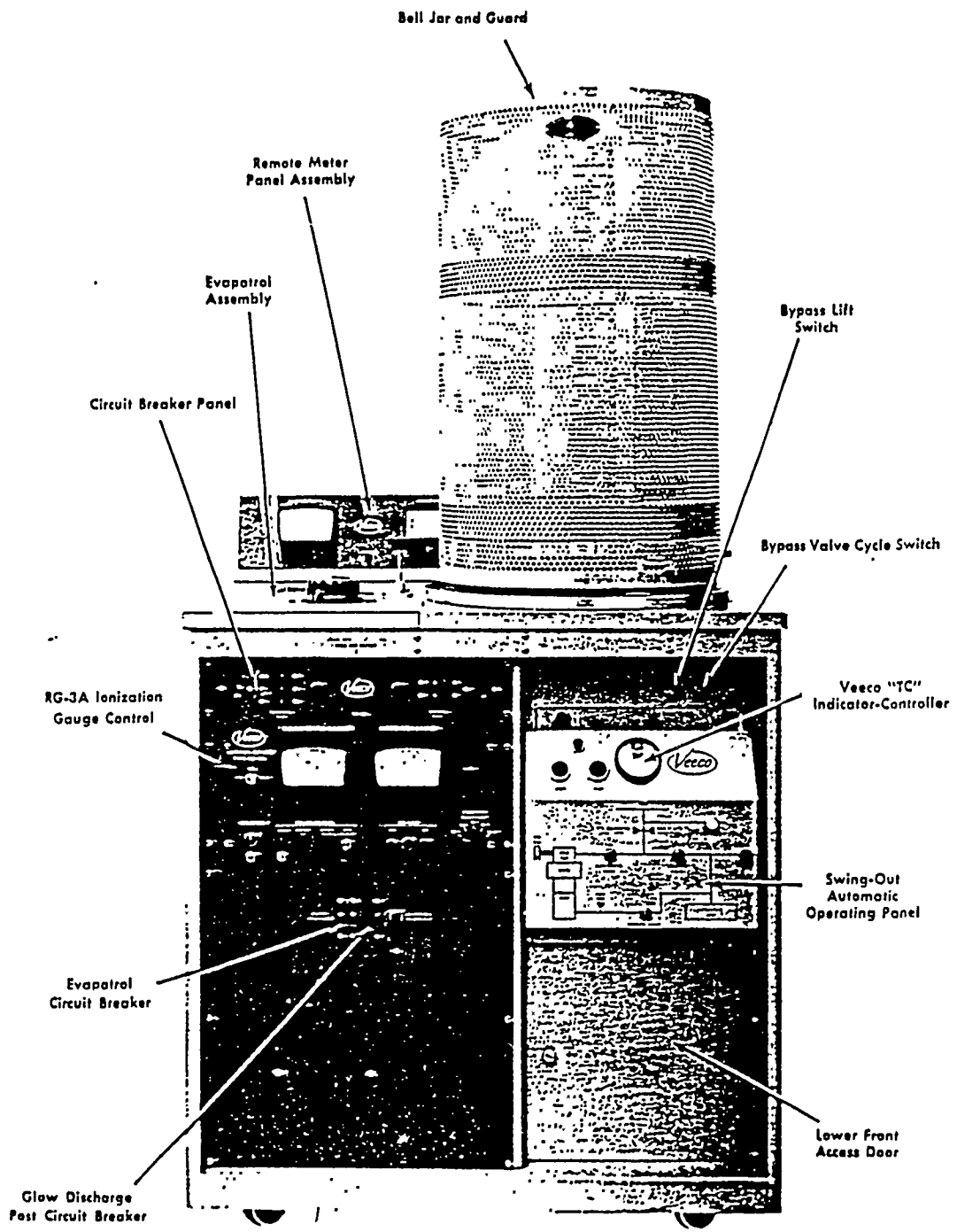


Figure 10. VE-401 Automatic High Vacuum Evaporator. [Ref. 8]

The pressure gauge controls consist of

- two standard thermocouple gauges capable of reading pressures from 1000 microns of mercury to the region of 1 micron of mercury;
- one thermocouple indicator-controller used to control the automatic functioning of the vacuum system;
- one Bayard-Alpert type ionization gauge capable of reading pressures from  $1 \times 10^{-3}$  torr to  $2 \times 10^{-9}$  torr.

The evaporator equipment consists of various transformers and connections necessary to provide high current (up to 500 amperes) to the boat or filament used to hold and melt the substance to be deposited.

*f. Deposit Thickness Monitor*

The SLOAN DTM-2A deposit thickness monitor [Ref. 9] was used to monitor the deposition process. The DTM-2A measures the mass of the deposit. The mass is measured by evaluating the change in frequency of a resonating quartz crystal as a deposit builds up on its surface.

The DTM-2A consists of a sensing unit, an operating unit and a connecting cable. The sensing unit is a transistorized, crystal controlled oscillator housed in a vacuum tight package. The operating unit is an all solid state device whose principle display of information is in the form of a precision meter movement but also utilizes an audio amplifier and speaker principally for calibration purposes.

Before deposition the variable frequency oscillator is tuned so that the beat frequency between it and the crystal oscillator is zero (it is here that the audio amplifier and speaker are used in order to achieve more accuracy). After zero tuning the variable frequency oscillator frequency is kept fixed. As soon as deposition begins the crystal frequency changes and a difference frequency is heard. As the deposit thickness becomes appreciable (30 Angstrom units of Aluminum) the meter will begin to indicate. As the deposit thickness becomes greater the beat frequency will also rise according to the equation

$$T = A \frac{\Delta F}{\rho} \quad \{32\}$$

where  $T$  = deposit thickness in Angstroms

$\Delta F$  = beat frequency in hertz

$\rho$  = bulk density of the depositing material in  $g/cm^3$

$A$  = a constant dependent upon the depositing material.

## 2. CO<sub>2</sub> Laser System

In order to produce a high intensity laser pulse, shape it and direct it onto a target under vacuum the following equipment was utilized: Lumonics CO<sub>2</sub> laser, various optics, a target chamber, and an energy meter with its associated probe.

### a. CO<sub>2</sub> Laser

Weston [Ref. 10] described the CO<sub>2</sub> laser in Figure 11 as follows:

"A Lumonics TE 822 HP high energy TEA pulsed laser was used as the laser source. It is capable of producing 20 joules of output and has an adjustable pulse width from 0.05 usec to 5.0 usec." "This laser uses an optically active medium of carbon dioxide, nitrogen, and helium, which is excited by a transverse electrical discharge. A population inversion results from the discharge electrons colliding with the CO<sub>2</sub> and N<sub>2</sub> molecules. Since one of the N<sub>2</sub> molecular upper vibrational levels possesses an excitation energy which is approximately equal to that of the CO<sub>2</sub> molecule, the N<sub>2</sub> serves to enhance the magnitude of the population inversion by the efficient transfer of vibrational energy during collisions between the CO<sub>2</sub> and N<sub>2</sub> molecules. Thus, the N<sub>2</sub> serves as reservoir of energy which directly influences laser peak power and pulse length.

"Helium is used to obtain a well diffused electrical discharge. The He also removes heat (generated by the electrical discharge) and lowers the gas mixture temperature. This results in less depletion of the CO<sub>2</sub> upper vibrational level, and the interaction of the CO<sub>2</sub> and He increases relaxation of the CO<sub>2</sub> lower vibrational level. Therefore, the use of He allows the laser to be pumped at higher discharge currents, which produces a larger population inversion and thus higher power. The high voltage power supply and gases were cooled by a Flowrite (RPCX mod 387) chill water unit with a flow rate of 25 gallons per hour at ..."[Ref. 10] 15 ± 5°C.

"The Lumonics laser with a multimode optic emits a 30 × 33 mm beam of approximately rectangular shape. The pulse shape can be varied in time from 0.05 usec to 5.0 usec by adjusting the gas mixtures. For a variety of reasons, a standard long pulse mixture, resulting in a 4.55 usec pulse was used ...." "The standard gas settings for long pulse are: 10 psig on the pressure gauges for CO<sub>2</sub>, N<sub>2</sub>, and He, 8 standard cubic feet per hour (SCFH) for CO<sub>2</sub> and N<sub>2</sub>, and 6 SCFH for He. This provided a reasonable pulse shape with a good distribution of the laser energy in time. The power density was varied by adjusting the voltage of the capacitor discharge ...."[Ref. 10]

### b. Target Chamber

The target chamber is shown in Figure 12. As described by Wojtowich [Ref. 11] it is

"The VEECO 400 vacuum system ... is utilized in conjunction with the CO<sub>2</sub> laser for research of plasma surface interactions at the Naval Postgraduate School. The system is a modified vacuum deposition system which has been refitted with a vacuum chamber. The vacuum pumping system consists of a mechanical pump, a water cooled diffusion pump, and a liquid N<sub>2</sub> cooled cold trap. The pressure range of the chamber is from 1.0 atmosphere down to 10<sup>-9</sup> atmospheres (atm). Three different gauges are required to determine the pressure in different ranges.

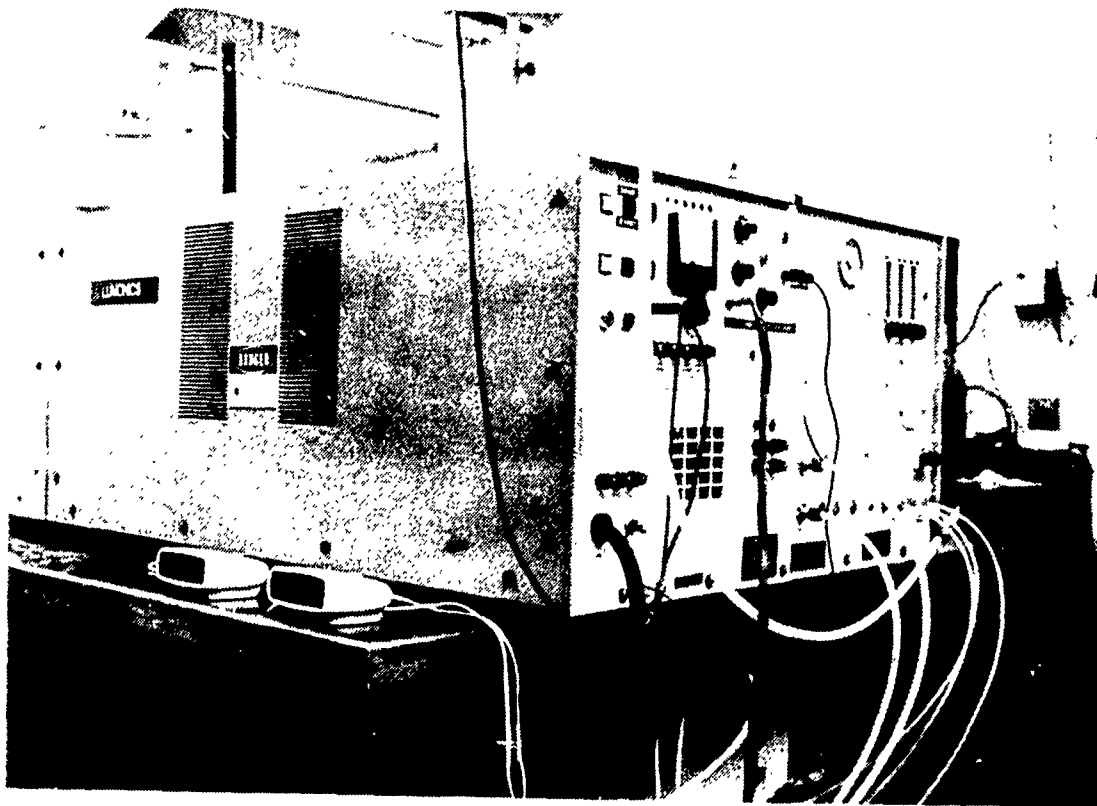


Figure 11. Lumonics TE-822HP CO<sub>2</sub> Laser

Pressures from one atmosphere (760 torr) down to 0.005 atmosphere (3.8 torr) are measured from a Matheson pressure gauge (model 63-5601) mounted on the top of the chamber; this gauge contains a Bourdon tube and socket .... Pressures between  $10^{-3}$  atmosphere (0.76 torr) and  $10^{-6}$  atmosphere ( $7.6 \times 10^{-4}$  torr) are measured by a thermocouple gauge located below the chamber. Pressures between  $10^{-6}$  atmosphere ( $7.6 \times 10^{-6}$  torr) and  $10^{-9}$  atmosphere ( $5.5 \times 10^{-6}$  torr) are measured by an ionization gauge located above the diffusion pump."

There were four ports into the target chamber, two were of metal and one was a NaCl window. The laser beam entered through the fourth port which was of ZnSe.

*c. Energy Meter and Probe*

The energy meter and probe used were clearly described by Henson [Ref. 12].

"The energy output of the laser was measured using the Laser Precision Corporation Model Rj-7100 energy meter with the Model Rjp-736 energy probe

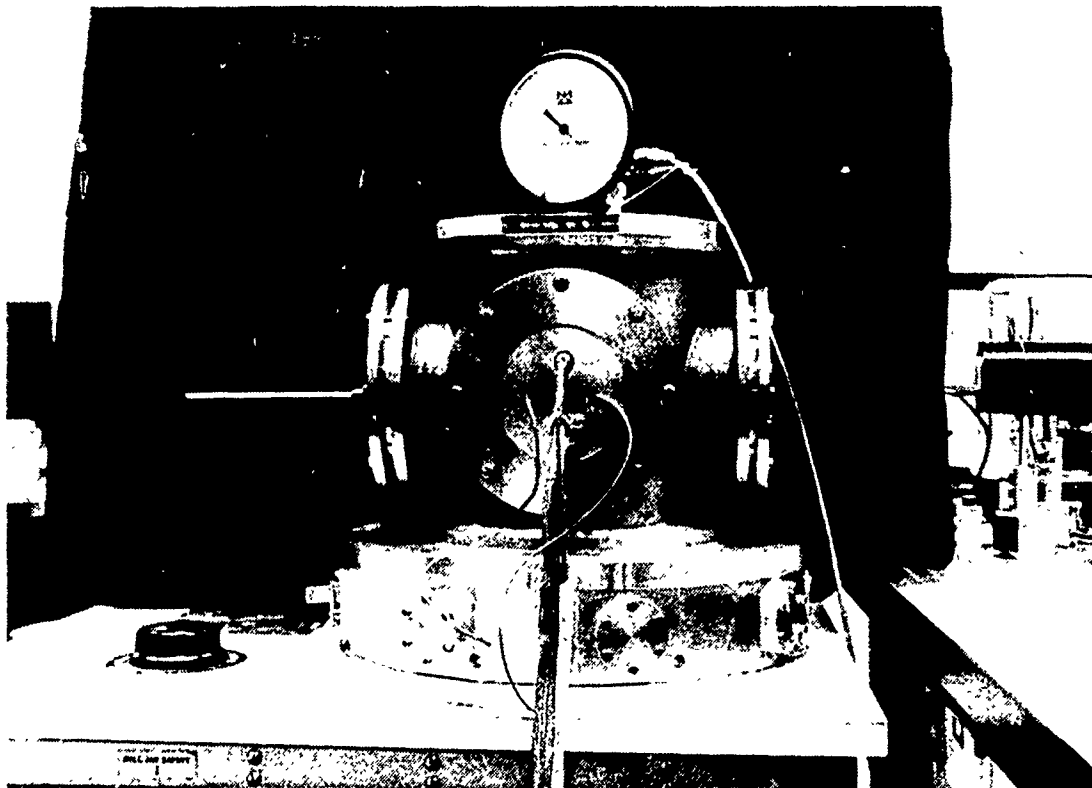


Figure 12. Target Chamber.

which is designed to detect laser pulses of wavelengths between 0.35 and 11.0 microns. The meter is capable of measuring the energy of a laser pulse of 1 nsec to 1 msec duration, and total energy ranging from 10 uJ to 10 J.... The energy detected at the probe is only a small percentage (0.13%) of the total energy of the laser pulse, whose flux on the target is calculated from the reflectance and transmittance of the ZnSe beam splitter, as well as the transmittances of the ZnSe focusing lens and ... ZnSe window.

*d. Optics*

The optics used to direct and focus the laser light are as follows:

- one 7.62 cm diameter ZnSe beam splitter with 99.38% reflectance, 0.13% transmittance, and 0.49% absorption at an incidence angle of 45 degrees;
- one 7.62 cm diameter ZnSe focusing lens with 98.5% transmittance, 0.26% absorption, and a 38 cm focal length;
- one 7.62 cm diameter ZnSe window with 98.0% transmittance.

### 3. Analysis Equipment

In order to analyze the surface of the targets the following equipments were utilized: optical microscope and a scanning electron microscope (SEM).

#### *a. Optical Microscope*

Preliminary analysis of target damage and investigation of the concurrent pitting was conducted using a Zeiss ICM 405 Inverted Camera Microscope (Figure 13) with reflecting light. This microscope allowed viewing and photography of surfaces in magnification powers of 50X, 100X, 200X and 500X.

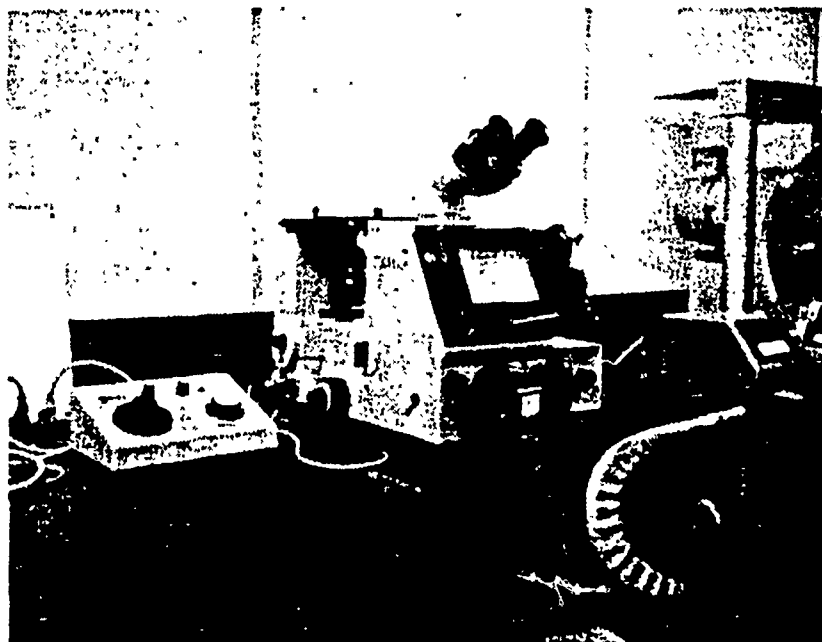


Figure 13. ZEISS ICM 405 Inverted Camera Microscope

#### *b. Scanning Electron Microscope*

Final target analysis was conducted using the Stereoscan 500 Scanning Electron Microscope [Ref. 13] which is capable of magnifications up to 280,000 X. Its basic function is to construct an image which has a three-dimensional appearance from the action of an electron beam scanning the surface. Under suitable conditions the re-

solution of this instrument can be better than 4 nanometers with a depth of focus at least 300 times greater than that of a light microscope at the limit of resolution.

A basic diagram of the SEM is shown in Figure 14. The SEM is constructed of five main components, these are

- "Electron Gun produces a large, high intensity electron beam which is fitted into
- the Column which controls and shapes the beam into a size useable for scanning microscopy.
- The Scanning System scans the beam over the sample in a television type raster. The beam scanning over the sample releases electrons from it.
- The Electron Collector Assembly collects these electrons and converts them to an image which can be viewed by the operator.
- The Control Electronics allows you to control the performance of items 1 to 4." [Ref. 13]

The only other capability of the SEM which was used for this thesis was its Elemental Analysis function.

"All samples will emit X-rays when struck by the electron beam. These X-rays are characteristic of the element from which they are emitted. By the use of special detectors sensitive to X-rays the sample may be analyzed for its constituent elements. The results may be either a plot of the concentration of the element present, or the spatial distribution of a chosen element on the sample surface. Particles as small as 1 micron may be analyzed." [Ref. 13]

## B. THE EXPERIMENTAL PROCEDURE

This section explains the methods used to calibrate the equipment, prepare the targets and conduct the shot.

### 1. Calibration

The only equipment item needing calibration by this researcher was the Deposit Thickness Monitor (DTM-3). Its calibration for copper is described below.

Since no multiple beam interferometer was available, calibration for copper was achieved by measuring the initial mass ( $0.3130 \pm .0001$  g) and surface area ( $3.61 \pm .1 \text{ cm}^2$ ) of the crystal, then depositing to a beat frequency of  $187.5 \pm .25$  kHz. The crystal mass was then again measured and found to be  $0.3265 \pm .0001$  g. The mass difference being .0135 g yields a film thickness of

$$\begin{aligned} T &= \frac{\text{mass}}{\text{area} \times \rho} \\ &= 4.178 \mu\text{m} \end{aligned} \quad \{33\}$$

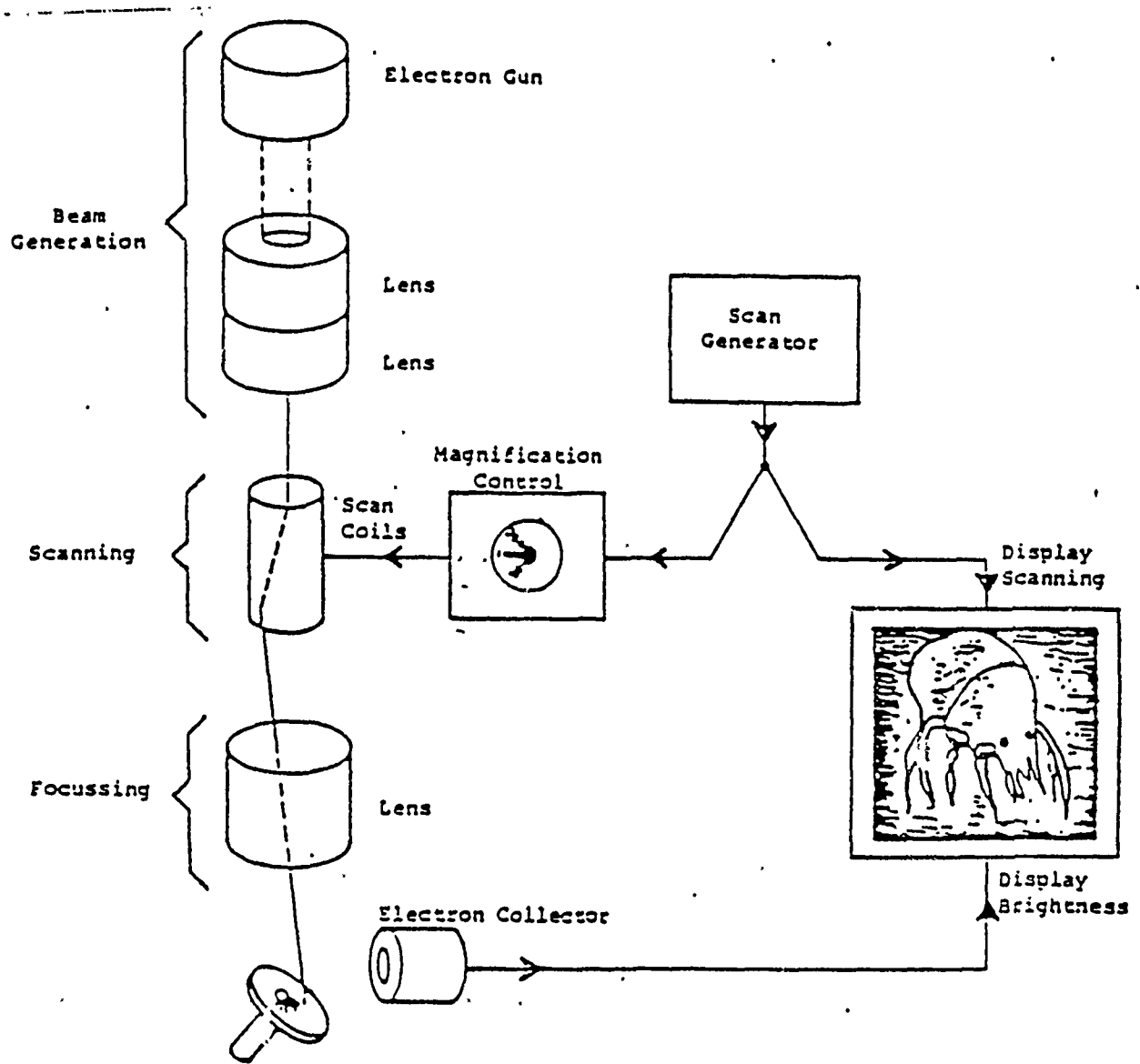


Figure 14. Basic Schematic Diagram of the Operation of the SEM. [Ref. 13]

Measurements on photographs of the crystal's edge (see Figure 15) reveal a thickness of

$$T \approx 4.0 \mu m \quad \{34\}$$

Taking the average value of these two results yields a thickness of

$$T = 4.089 \mu m \quad \{35\}$$

Manipulation of equation (32) thus yields the constant for copper to be

$$\begin{aligned} A &= \frac{\rho \times T}{\Delta F} \\ &= 1.952 \pm .003 \end{aligned} \quad \{36\}$$

and so the equation for determination of the thickness of the copper deposits is

$$T(\text{\AA}) = 1.952 \times \frac{\Delta F(\text{Hz})}{\rho(\text{g/cm}^3)} \quad \{37\}$$

with the density of copper being  $8.95 \text{g/cm}^3$ . This equation is used throughout this thesis as the sole source for the determination of the film thicknesses.

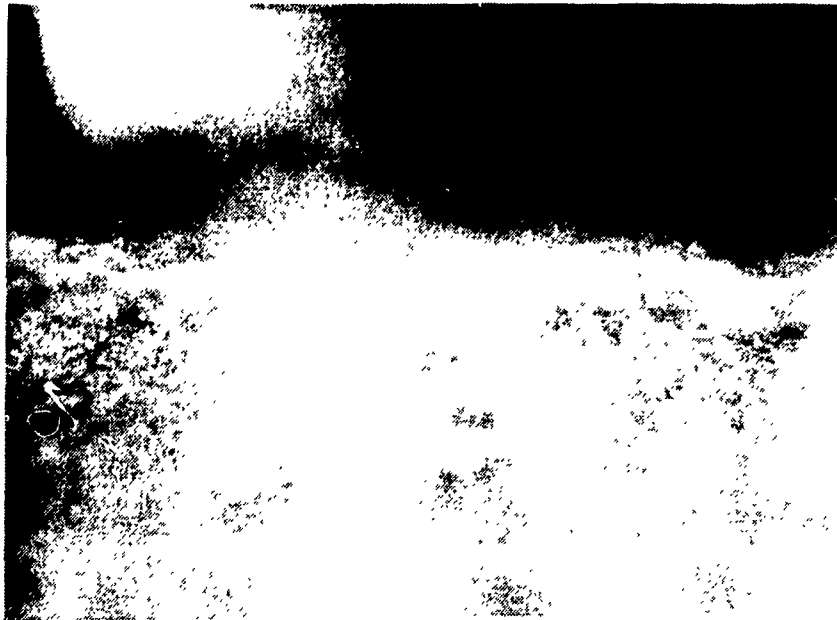


Figure 15. 500X Photograph of the DTM Crystal's Edge after Deposition.

## 2. Target Preparation

The following procedure was developed using standard microscope slides. Films were deposited onto these slides using various preparation and deposition techniques and then the film was analyzed. This analysis consisted of scrutiny under an optical microscope and also the placement of a light source on one side while looking for light leaks (holes) on the other. Correlation between these two methods of analysis yielded the general characteristics of film defects to be easily discernable from pitting caused by Unipolar Arcing. The techniques mentioned below yielded the best results, fewer than 10 significant defects over an approximate area of  $5 \text{ cm}^2$ .

The target substrate was manufactured from one-half inch diameter type 304 stainless steel rod which was cut into one centimeter sections. One face of these cylinders was polished to the extent obtainable with .05 micron Alumina using standard polishing techniques.

In order to deposit a fine quality film it is necessary for the surface to be exceptionally clean and free of all loose particles and dust (most of these particles have a much larger diameter than the thickness of the film). To obtain this necessary level of cleanliness the targets were first cleaned ultrasonically in an acetone bath. Further cleaning was done in a clean air environment produced by the Pure-Air system. In this clean environment the targets were dipped into acetone and then into ethyl alcohol, scrubbed with a standard drugstore variety toothbrush and dipped again. Since both the acetone and the ethyl alcohol contain particulate impurities the targets were also suspended above a boiling solution of acetone and ethyl alcohol in the Vapor Degreaser, thus the targets were cleaned further by distilled acetone and ethyl alcohol which condensed onto their surfaces and ran off by gravity. All transport of the targets after being in the Pure-Air system was conducted inside of a clean, sealed metallic box.

After cleaning the targets were placed inside of the VEECO VE-401 Automatic High Vacuum Evaporator and allowed to outgas under high vacuum (approximately  $6.0 \times 10^{-7}$  mm Hg) for about one hour. The targets were placed 17 centimeters above the evaporation boat (hereafter simply referred to as boat). The DTM-3 oscillator was placed at the same height as the targets and equidistant from the point directly above the boat. The boat used was made of tungsten, it and its characteristics are shown in Figure 4.

Before the 99.9% pure copper in the boat is heated a shield is placed over the boat to prevent deposition of impurities onto either the targets or the DTM-3 Oscillator. Current through the boat was slowly raised to 100 amperes. This raises the boat tem-

perature to just above the melting point of the copper (1083 °C). After allowing all of the copper to become molten the current was further raised to 130 amperes. One minute more was allowed for the system to reach steady state and allow any impurities or released particles to settle. The shield was then removed allowing the vapors from the molten copper to deposit onto the targets and the DTM-3 Oscillator. The deposition was constantly monitored using the DTM-3 and when the desired change in frequency (and thus thickness) was achieved the shield was inserted and the current reduced to zero. A one hour cooldown under high vacuum (about  $6.0 \times 10^{-7}$  mm Hg) was allowed before the target was removed. These films were then analyzed under the optical microscope and their quality noted.

The laser shot onto the target was conducted with the setup shown in Figure 16. The target was placed under a vacuum in the  $10^{-5}$  mmHg range and shot with a focused 4.55 $\mu$ sec laser pulse.

Final analysis was conducted with the use of the SEM. The smallest pitting that penetrated through to the stainless steel and the largest pitting which did not penetrate was photographed as was their X-ray elemental analyses.

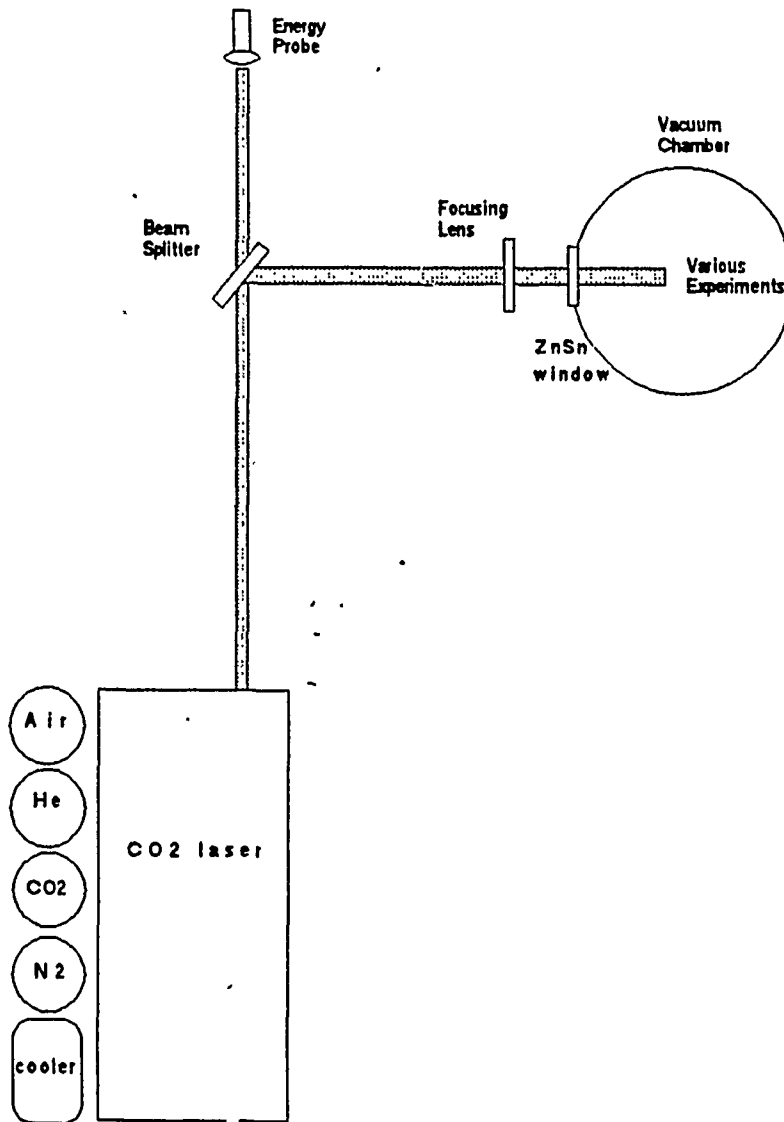


Figure 16. Equipment Configuration for the Laser Shot.

## IV. EXPERIMENTAL RESULTS AND DISCUSSION

This chapter reports the results of the experiments undertaken and gives an analysis of their implications. The beginning describes the results of experiments to determine the direction of emission of bulk material during the laser-target interaction. Structure was found in this emitted material by studying how it deposited onto a highly polished surface. This was followed by investigating damage to thin copper films on highly polished stainless steel targets. Damage to these films led to a method of calculation of the arc current using basic thermodynamic principles. Finally, the results of experiments to find a relation between the size of the pits and their depth is given.

### A. INITIAL INVESTIGATIONS

This section reports the results of experiments conducted to determine the direction of emission of bulk material during unipolar arcing. It also presents the results of deposition of this material onto a highly polished stainless steel target.

#### 1. Normal Emission of Bulk Material

The first part of this research involved study of the material ejected from the surface by unipolar arcing. Specifically, this section deals with finding out if there is any directional dependence to the emission of bulk material.

Unless acted upon by external forces, such as electric and magnetic fields, a plasma, once produced, is expected to expand fairly uniformly to fill the vacuum and finally to deposit onto the surfaces of the chamber. To get a rough idea of the bulk distribution of the material ejected when the laser strikes the target the following experiment was conducted. A hole was made in a piece of aluminum foil and the foil placed normal to a copper target as shown in Figure 17. The hole was made to allow the laser pulse to penetrate and normally strike the target. The experiment was placed in a vacuum of  $2.0 \times 10^{-4}$  mmHg and shot with the laser 60 times at 1 Hz. Average pulse energy was 17.0 Joules. There was no visible copper deposited onto the foil.

Investigating further it was found that keeping the foil parallel to the target surface but having the laser pulse come in at an angle (as in Figure 18) produced significant deposition. The parameters for this shot were the same as before, the only exception being that the energy meter read an average pulse energy of 18.1 Joules. A qualitative examination of the deposition showed that most of the deposition occurred directly over the laser spot on the target. Different laser entrance angles produced the

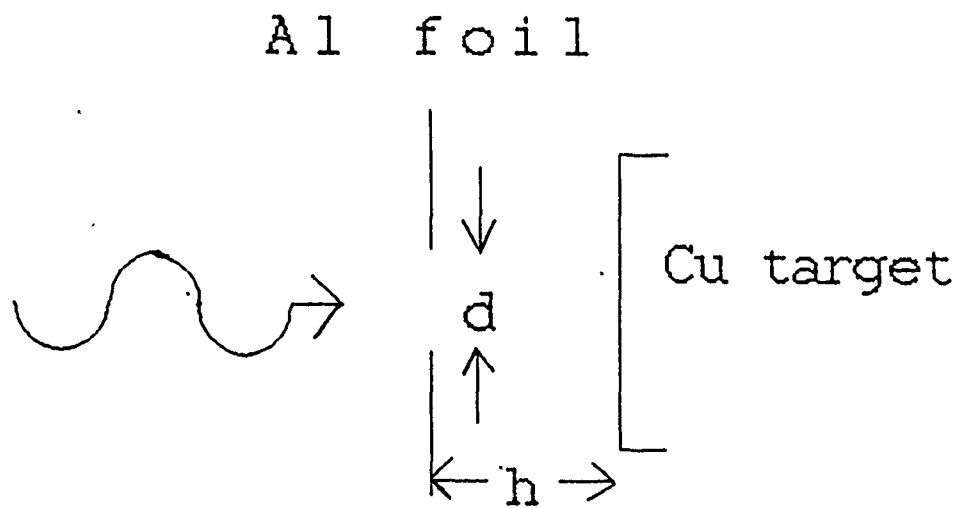


Figure 17. Diagram of first experiment to determine the directionality of material emission from a copper target.:  $d = 3 \pm 1mm$ ,  $h = 2.3 \pm 0.3cm$

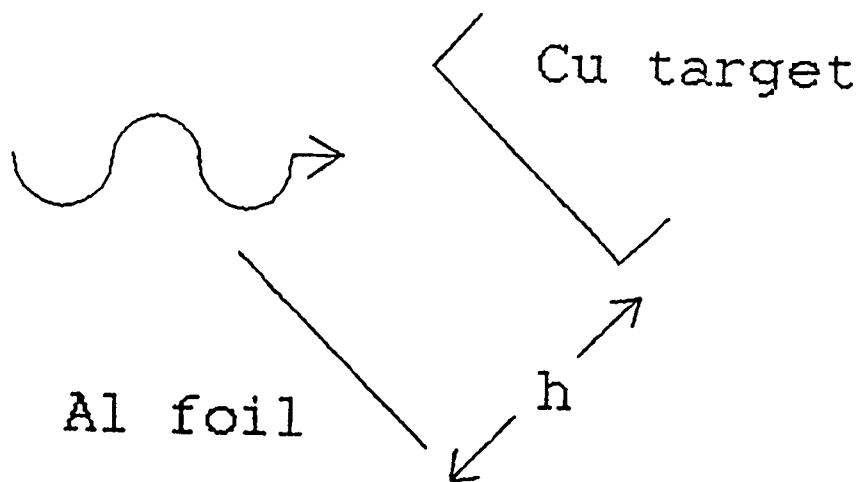


Figure 18. Diagram of second experiment to determine the directional dependence of material emission from a copper target.:  $h = 1.7 \pm 0.2 cm$ .

same results. These experiments indicate that during the laser target interaction the bulk of the material which is emitted is emitted normal to the target surface. It will be shown later that this should be universal for unipolar arcing.

## 2. Deposition profile of ejected bulk material

To further investigate this ejected material the aluminum foil was replaced with a highly polished type 304 stainless steel surface. The idea being that the ejected material, whether it was metallic vapors, plasma or molten liquid, would adhere to the surface. How it adhered would indicate the extent of the directionality and any structure that may be present.

In the first experiment the system was placed under a vacuum of  $4 \times 10^{-3}$  mmHg. The laser target was then shot with 60 pulses at a frequency of 1 Hz. The average energy of each pulse was 17.1 Joules, and the distance between the copper target and the steel surface,  $h$ , was  $1.4 \pm 0.1$  cm. Visual examination of the steel surface revealed the same results as with the aluminum foil. There was significant copper deposition normal to the laser spot of roughly the same size and shape (see Figure 19). Beyond this deposition region there was some spotted deposits of copper with the rest of the surface being covered with a blue film. This blue film indicates a deposition thickness of 100 to 200 nanometers over the rest of the surface.

Examination under an optical microscope revealed several interesting phenomena. Figure 20 reveals significant pitting occurring in the region of dense copper deposition with the amount of pitting decreasing with the amount of deposition. This indicates that a hot and dense plasma is being emitted normally from the target surface and not expanding very rapidly in the radial direction.

Figure 21 and Figure 22 reveal an intriguing ring structure found at two places on the edge of the region of dense deposition. This was also found in other shots to be described later. A possible explanation will be given then.

Examination of the region outside of the dense deposition revealed circular copper deposits (Figure 23). There are no pits in these deposits. They are circular and appear to be fairly uniform. Each of these deposits are most likely caused by either the emission of a jet of copper vapor from a single unipolar arc occurring on the laser target surface or droplet formation (or some combination of the two).

Reducing the vacuum to  $5.3 \pm 0.5$  mmHg while leaving all of the other parameters essentially constant produced very little deposition. However, it did produce significant pitting in the steel surface as shown in Figure 24, Figure 25 and Figure 26. The phenomenon of rings formed around pits is also clearly evident. The figures show that



Figure 19. Steel surface showing bulk copper deposition. (6.4X)( $\longleftrightarrow$  1.0mm)

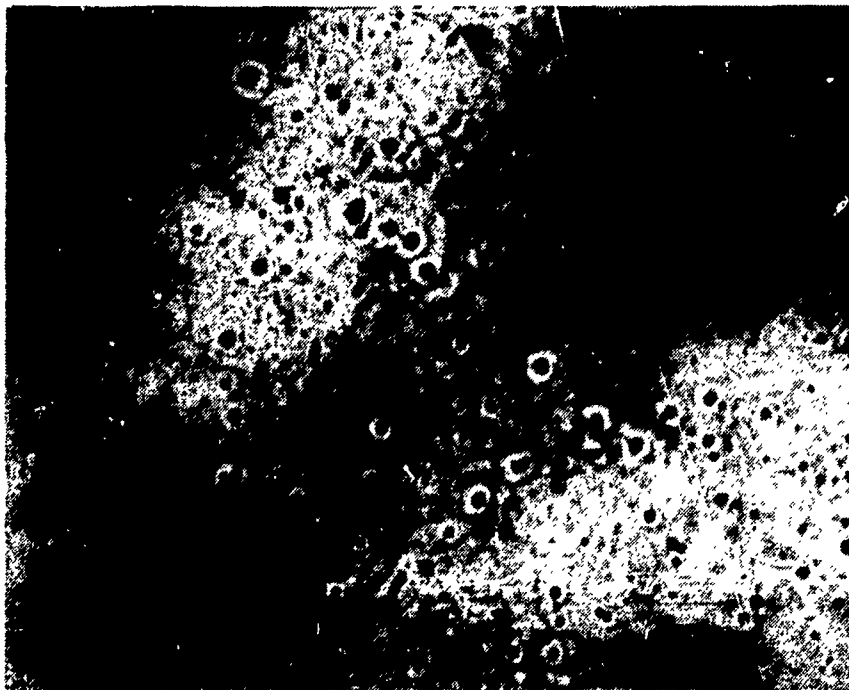


Figure 20. Copper deposition on a steel surface showing a correlation between greater pitting density with greater copper deposition. (200X)  
( $\longleftrightarrow$  50 $\mu$ m)

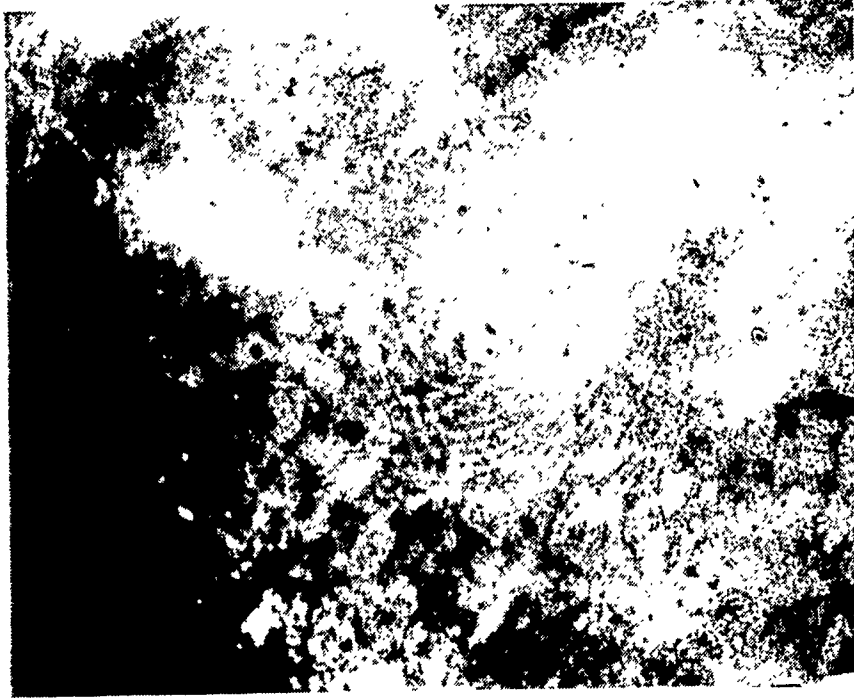


Figure 21. Ring structure: found surrounding a pit at the edge of the dense copper deposition region in Figure 19.(200X) ( ——— 50 $\mu$ m)

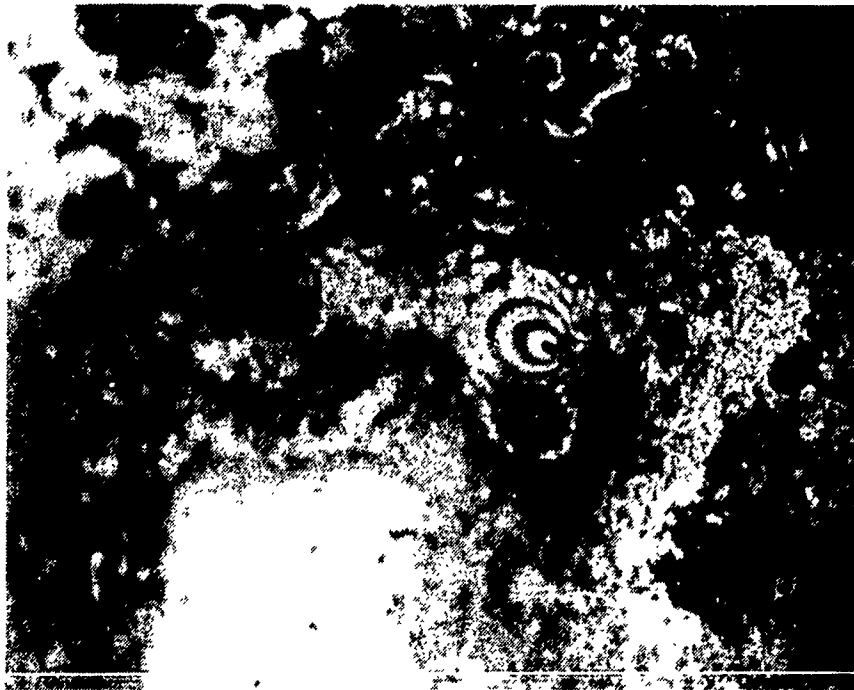


Figure 22. Second ring structure: found surrounding a pit at the edge of the dense copper deposition region in Figure 19.(200X) ( ——— 50 $\mu$ m)

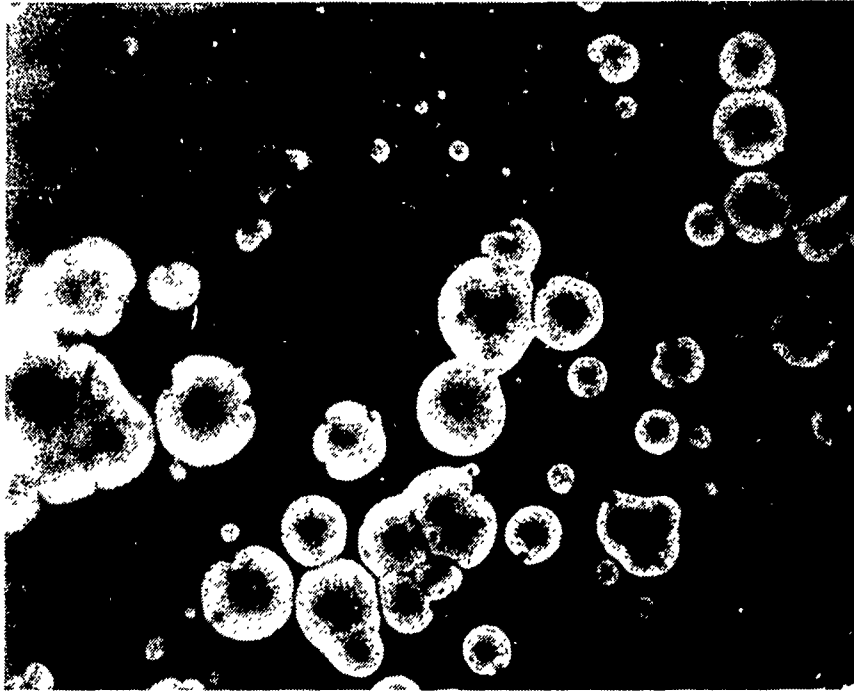


Figure 23. Circular copper deposits: found outside of the region of dense deposition in Figure 19. (500X) (— 20 $\mu$ m)

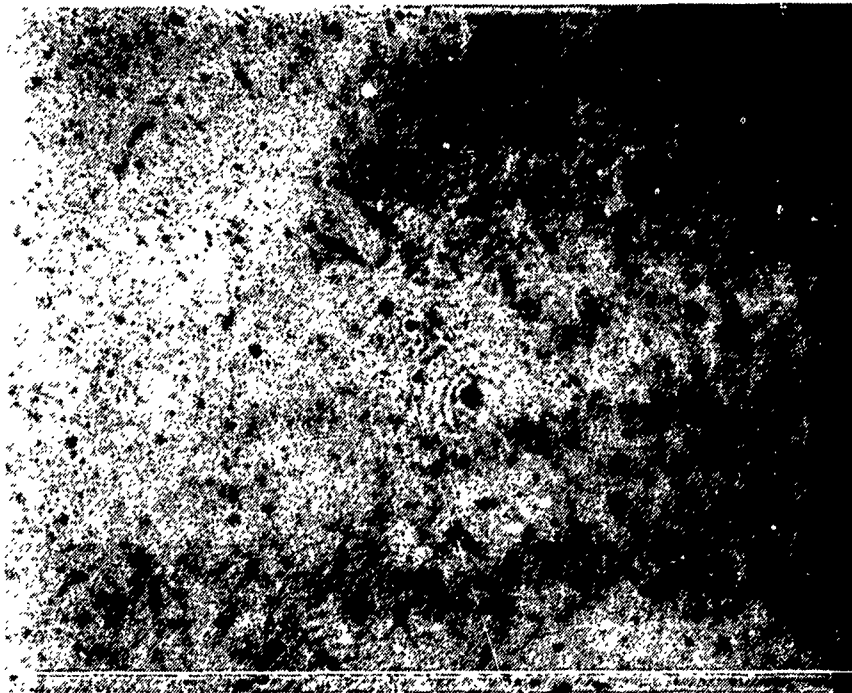


Figure 24. Interference deposition pattern: found on a polished steel surface subjected to a copper plasma. (200X) (— 50 $\mu$ m)



Figure 25. Second interference deposition pattern: found on a polished steel surface subjected to a copper plasma.(200X) (  $\longleftrightarrow$  50 $\mu$ m)

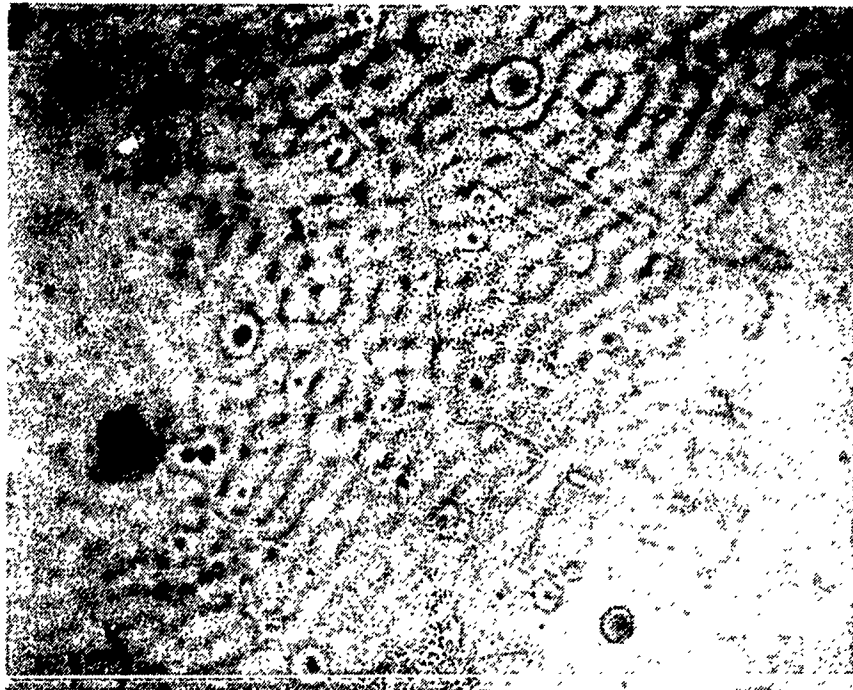


Figure 26. The region shown in Figure 25 at 500X. (  $\longleftrightarrow$  20 $\mu$ m)

these rings form interference patterns when their central pits are close enough for them to interact. Figure 26 is a higher magnification view of Figure 25 and shows that these ring interference patterns are made up of many small dots of deposition.

Further experiments did not yield such significant deposition as in Figure 19, however two deposition patterns were always evident: ring deposition and simple deposits. Observations with the optical microscope reveal that every deposit is surrounded by a light to dark blue film (as mentioned previously). This blue film is represented on these black-and-white photographs as the dark region surrounding the deposits. The data for Figures 27 through 33 are given in Table 1. In each shot the target was hit 60 times (at 1 Hz) by the CO<sub>2</sub> laser. The results of shot C were especially interesting. The surrounding blue regions of the deposits spread out in comet like tails with all of their heads directed towards the same central region.

Table 1. DATA FOR SHOTS A THROUGH D.

Shot	Vacuum (10 <sup>-5</sup> mmHg)	h (cm)	Average pulse en- ergy (J)
A	2.3	1.8 ± 0.1	21.9
B	2.8	1.8 ± 0.1	19.9
C	3.8	1.3 ± 0.1	20.6
D	3.5	1.3 ± 0.1	21.6

These experiments show that the bulk of the material ejected from the laser spot is emitted normal to the target surface. While some of this material expands into the vacuum most of it comes out in jets. Pitting on the steel surface indicates that this material contains plasma but it also contains a significant amount of neutral metal vapors. The wave structure is most likely caused by an oscillation in the incoming material which was generated by the central arc. Should this be the case, then the question of whether the rings are formed by an outward propagating disturbance produced by a single arc or an oscillating arc arises. Also, if the velocity of these waves could be measured or calculated, then the period of the unipolar arc could be directly measured from the period of the rings. This would have to be taken up in later study.



Figure 27. Shot A: Centers are copper deposits surrounded by yellow, and light and dark blue films on a copper background.(200X) (  $\text{---}$  50 $\mu\text{m}$ )

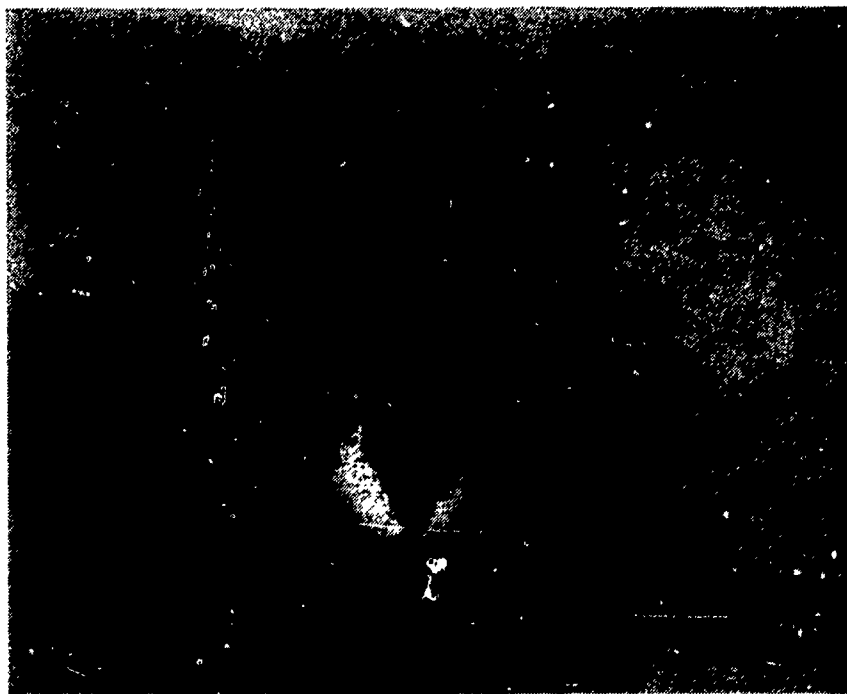


Figure 28. Shot A: The center is a copper deposit. The copper rings are on a blue background.(200X)(  $\text{---}$  50 $\mu\text{m}$ )



Figure 29. Shot B: This shows copper rings on a dark blue background (dark region). (200X)( $\longleftrightarrow$  50 $\mu$ m)

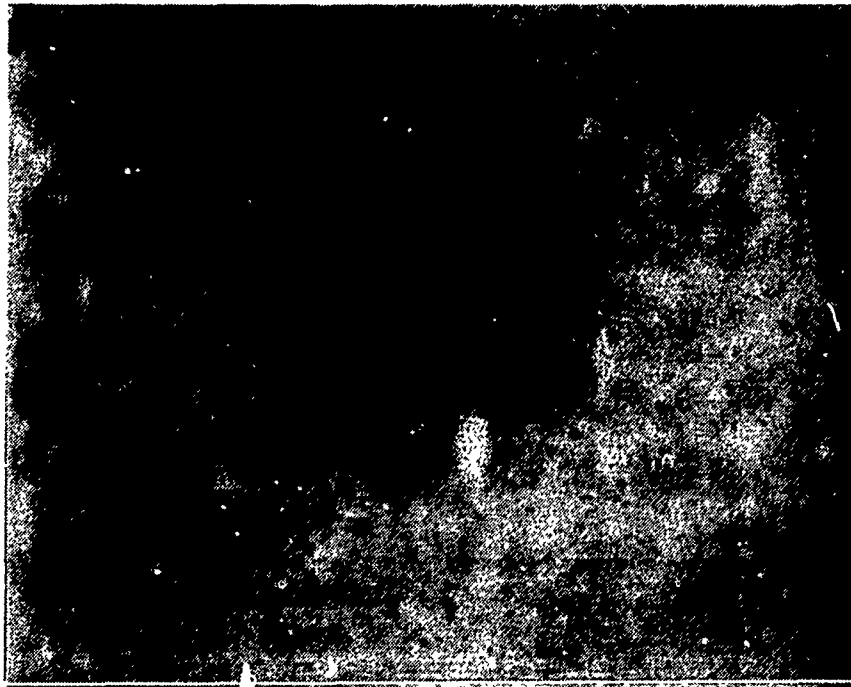


Figure 30. Shot C: The center towards which the other deposits in this shot point. (200X)( $\longleftrightarrow$  50 $\mu$ m)

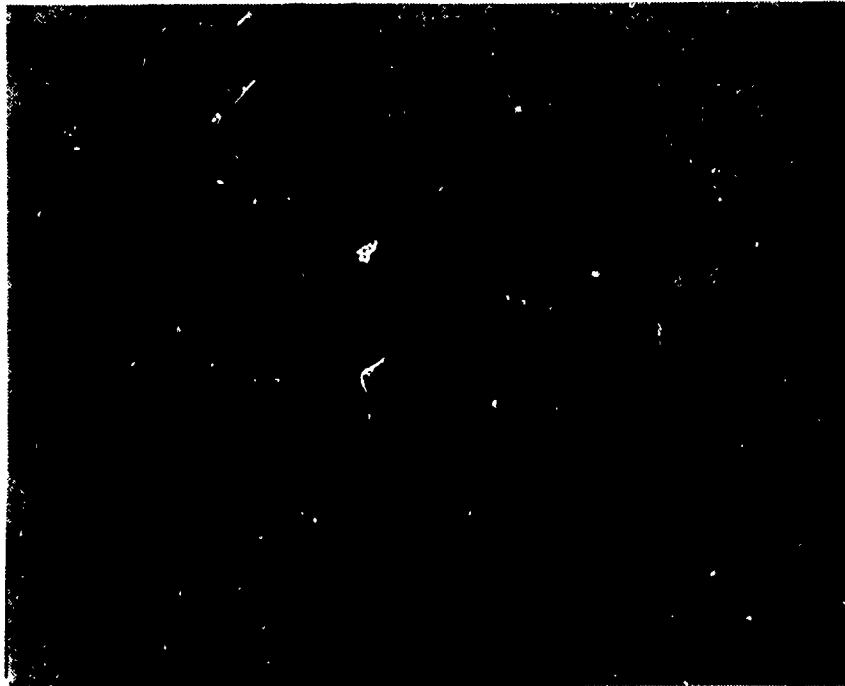


Figure 31. Shot C: Ring deposition with the background pointing towards Figure 30.(200X) (  $\longleftrightarrow$   $50\mu m$  )

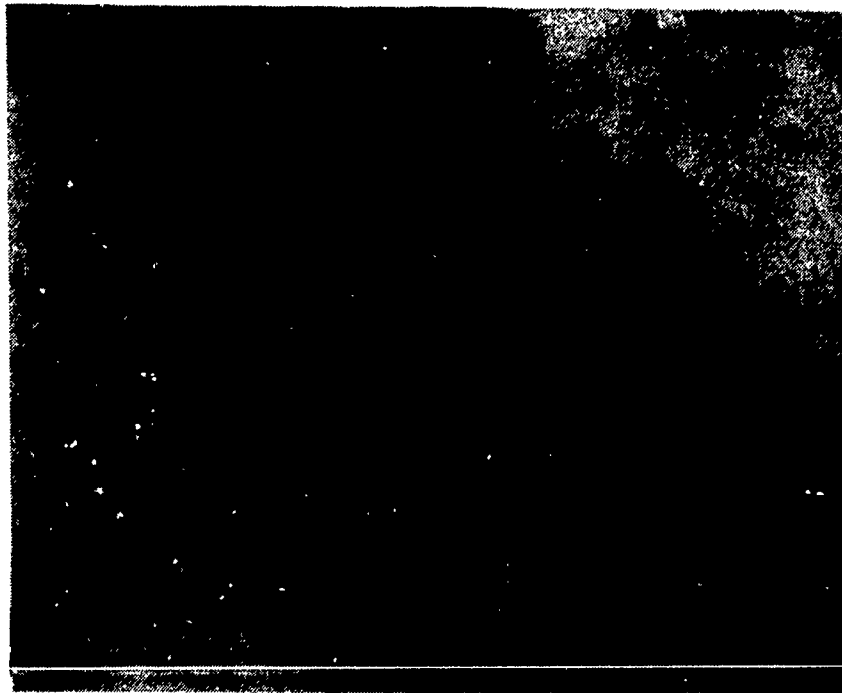


Figure 32. Shot C: Ring deposition with its background pointing towards Figure 30.(50X) (  $\longleftrightarrow$   $0.2mm$  )



Figure 33. Shot D: These are simple copper deposits with the usual blue surrounding film, the center is out of focus and steeply raised. (200X)  
( $\longleftarrow$  50 $\mu$ m)

## B. THIN FILMS AND THE UNIPOLAR ARC

Placing a thin film of copper onto a highly polished stainless steel target provides information on how the same unipolar arc affects the two different metals. This section begins by providing data from these experiments further enforcing the argument that the primary surface damage mechanism is simply local heating by the arc current. Specifically, the unipolar arc acts to melt and vaporize the surface in an isolated region. A detailed theoretical description of the dynamics of this process is given in Chapter V. Lastly, this information, along with some basic thermodynamics, is used to estimate the arc current. The last section provides preliminary data for establishing a correlation between a pit's depth and its width.

### 1. Arc damage - a heating phenomenon

To study the effect of the same laser shot, and the same unipolar arc, on two different materials a 0.37 micron copper film was placed over half of a type 304 stainless steel target. The target had been polished to the degree obtainable by 0.05 micron Alumina. This target was shot in a vacuum of  $3.5 \times 10^{-5}$  mmHg. Optical and scanning electron microscope analyses of damage in the laser spot revealed that while the copper

film was penetrated, the copper appeared to have been pushed aside (Figure 34 to Figure 37). This was even more apparent in the damaged areas outside of the laser spot. Figure 38 and Figure 39 show areas where the copper film was melted and somehow pulled radially outwards with no damage to the underlying steel. They also show regions where the underlying steel also suffered pitting yet the molten steel did not travel so far as did the molten copper.

These results are what would be expected given that the dynamics of the process is an electric arc joule heating and melting the material in a small region. This molten material then being acted upon by a radial force. The melting points of copper and iron are  $1083^{\circ}\text{C}$  and  $1535^{\circ}\text{C}$  respectively. Thus, for a given amount of heat placed over a short period of time, the copper would be expected to melt sooner and remain molten longer as it passed over a surface than would the iron (steel).

## 2. Calculation of Unipolar Arc Current

Assuming that the driving mechanism of the surface dynamics is produced by joule heating, then a rough calculation of the arc current is possible. This section will use some basic thermodynamics to develop a formula for this arc current. Since the currents of the unipolar arcs are most likely different as a function of time, this formula

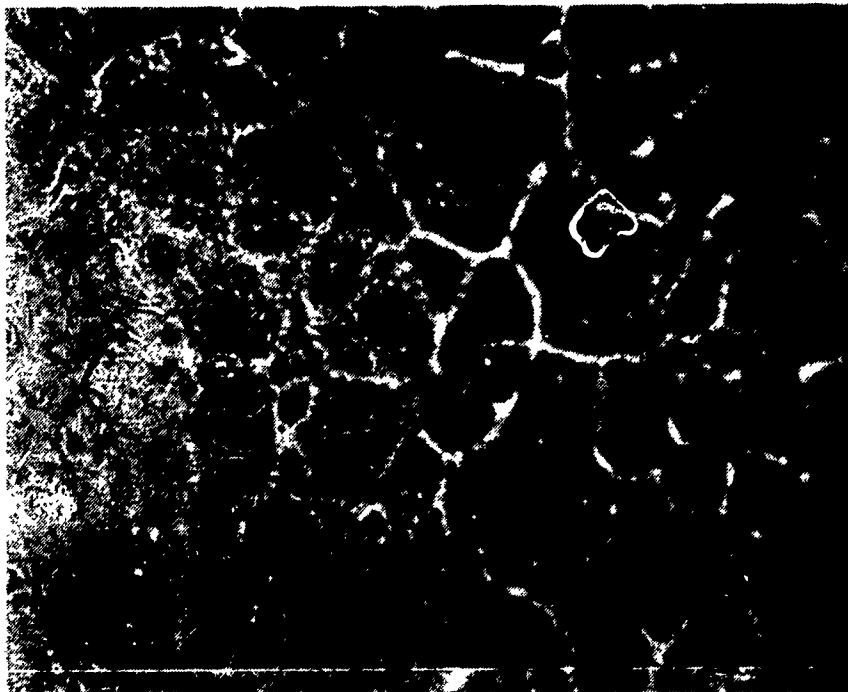


Figure 34. Optical microscope image of a focused laser spot: steel target overlaid with a 0.37 micron copper film.(500X) (single shot)( $\text{—}$  20 $\mu\text{m}$ )

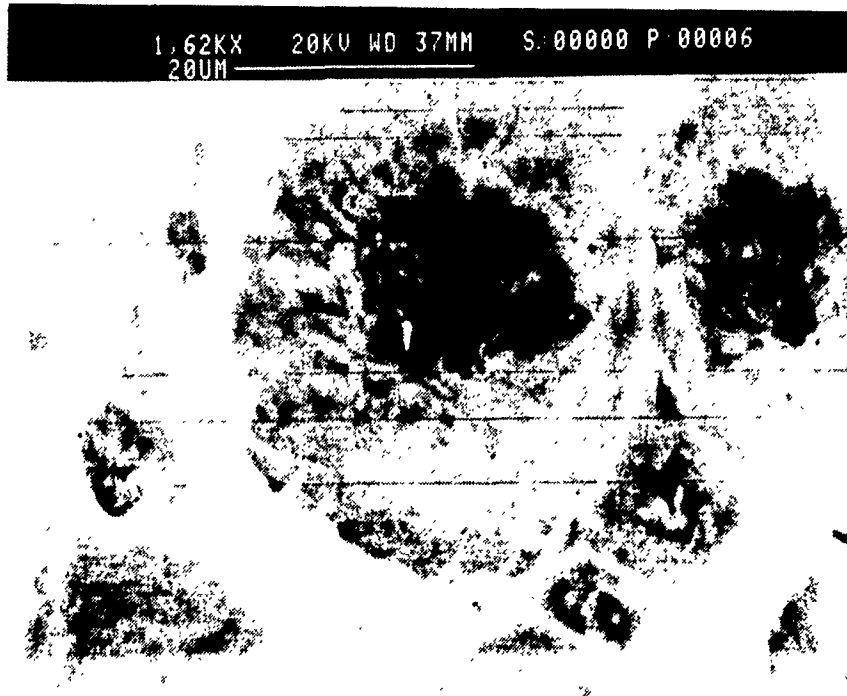


Figure 35. SEM image of laser spot.: same target as Figure 34.(1620X)

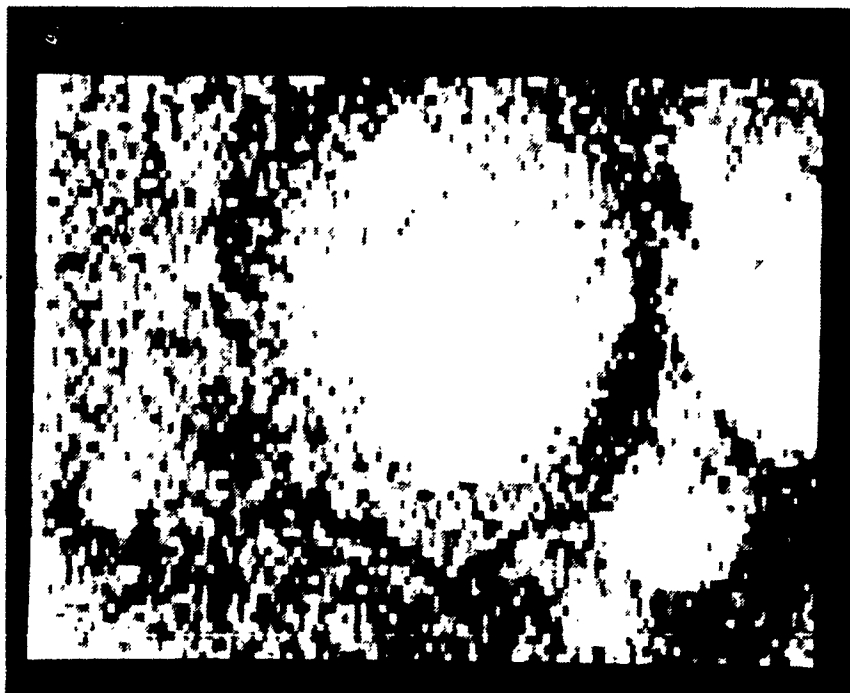


Figure 36. Distribution of iron in Figure 35.



Figure 37. Distribution of copper in Figure 35.

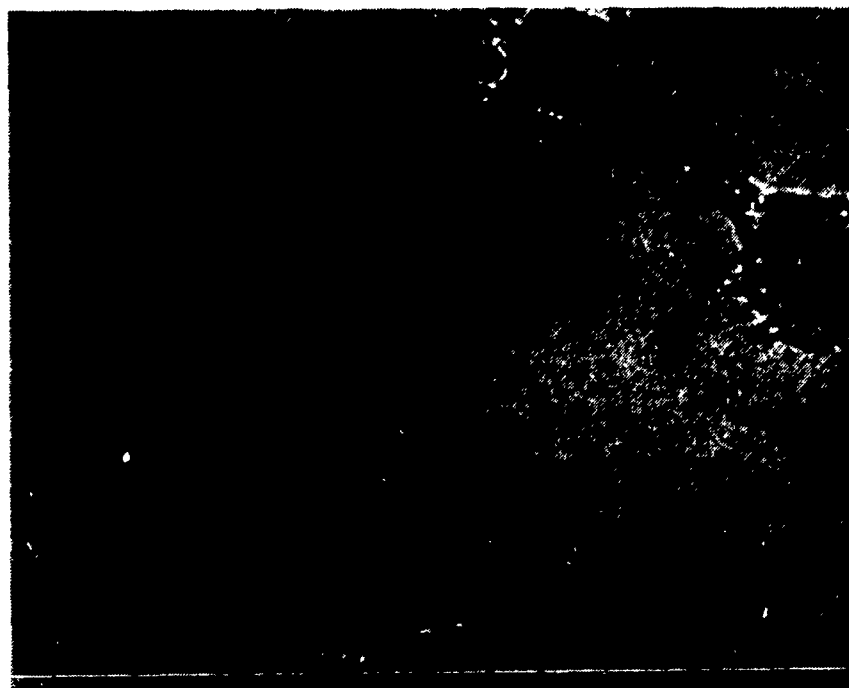


Figure 38. Optical microscope image of damage outside the laser spot: steel target overlaid with a 0.37 micron copper film. (500X) ( — 20 $\mu$ m)



Figure 39. Optical microscope image of further damage outside the laser spot: steel target overlaid with a 0.37 micron copper film. (500X)  
( $\longleftarrow$  20 $\mu$ m)

is only meant to provide an order of magnitude estimate of the average arc current. In light of this fact, several assumptions are made to simplify the calculations and the formula. Lastly, a calculation will be performed using an actual pit.

Assuming that the pit is cylindrical with radius  $r$  and depth  $h$ , then the mass in the pit is

$$m = \rho \pi r^2 h \quad \{38\}$$

where  $\rho$  is the density (8.95g/cm<sup>3</sup> for copper). The amount of heat necessary to melt all of this and to vaporize one-quarter of it is

$$Q_h = m(C_s \Delta T_s + L_f + C_l \Delta T_l + 0.25 L_v). \quad \{39\}$$

Where  $\Delta T_s =$  temperature change from initial temperature to melting point  
(1063°C for copper initially at 20°C)

$\Delta T_l =$  temperature change from melting point to vaporization point

$C_s =$  heat capacity for the solid (.092cal/g°C for copper)

$C_l =$  heat capacity for the liquid (0.118cal/g°C for copper)

$L_f =$  latent heat of fusion (49 cal/g for copper)

$L_v =$  latent heat of vaporization (1250 cal/g for copper).

Here the heat capacities are assumed to be constant over their respective regions. This assumption is fairly accurate over the regions given and should not be a significant source of error. Another assumption is that one-quarter of the material in the pit is vaporized. This is simply a very rough estimate which comes from observations as in Figure 39 and Figure 19. Figure 39 shows that a lot of material is going into the formation of the rim, whereas Figure 19 appears to show that a significant portion of the material in the pit is ejected. This assumption may be an order of magnitude source of error since the energy required to provide the latent of vaporization for all of the copper in the pit is eight times that required to heat it to its boiling point (1118°C in a vacuum of  $7.6 \times 10^{-4}$  mmHg). The factor of one-quarter was chosen to account for both the observed bulk material emission and the observed rim (which indicates that most of the material remained). The actual value of this factor is unknown.

In joule heating the power, P, provided by the arc current, I, is given by

$$P = I^2 R. \quad \{41\}$$

R is the resistance over the current path and is given by

$$R = \rho_r \frac{h}{\pi r^2} \quad \{42\}$$

where  $\rho_r$  is the resistivity ( $1.7 \times 10^{-8} \Omega \cdot m$  for copper). For simplicity the resistivity is assumed constant.

Since power in this case is the rate of production of energy, and heat,  $Q_h$ , is energy, then

$$\begin{aligned} Q_h &= Pt \\ &= I^2 Rt. \end{aligned} \quad \{43\}$$

Here  $t$  is the lifetime of the arc. It will be assumed that the current is constant throughout its lifetime and zero at any other time. A further assumption is that all of the heat produced by the arc goes into melting and vaporizing the metal in the pit. Of all of the assumptions in this derivation this is the one most subject to question. Copper's high thermal conductivity assures that heat will be transmitted into the surrounding metal. Taking this heat loss into account would severely complicate this derivation and so that must be left for further research.

Finally, combining equations (42) and (43) provides the formula for the arc current

$$I = \sqrt{\frac{\pi r^2}{h \rho_r} \frac{Q_h}{t}} \quad \{44\}$$

The current density is then simply

$$\begin{aligned} j &= \frac{I}{\pi r^2} \\ &= \sqrt{\frac{Q_h}{\rho_r \pi r^2 h t}} \end{aligned} \quad \{45\}$$

These equations should be fairly accurate for any arc in any material.

Figure 40 displays the unipolar arc pit which will be used in the following calculation of an arc current. The film thickness,  $h$ , is 1.89 microns, the pit radius,  $r$ , is 3.0 microns. Given these parameters and making the assumption that the arc lifetime is one microsecond the heat required is

$$Q_h \approx 9.32 \times 10^{-7} \text{ J.} \quad \{46\}$$

The arc current is then

$$I \approx 28.6 \text{ Amps.} \quad \{47\}$$

This value is very near the current assumed by Schwirzke [Ref. 4, p. 611] and that required by Wieckert [Ref. 14, p.500] providing further confirmation to their theories. The current density is

$$j \approx 1.01 \times 10^8 \text{ Amps/cm}^2. \quad \{48\}$$

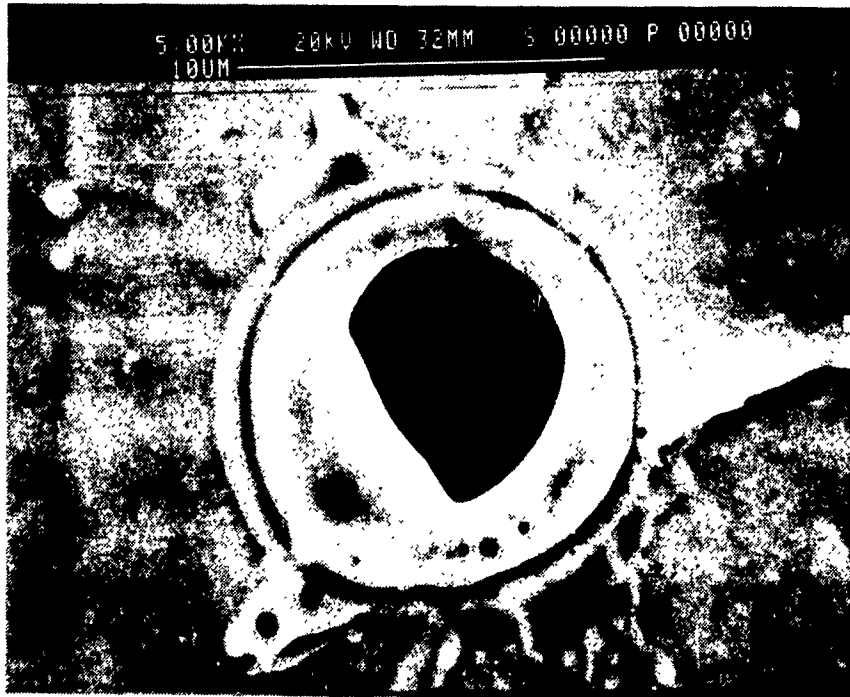


Figure 40. Calculation data: SEM photograph of unipolar arc pit fully penetrating a 1.89 micron copper film. (5000X)

This value is an order of magnitude below that required by Weickert [Ref. 14, p.500]. This is most likely due to the copper having moved radially away from the central arc as has been observed in the previous section, i.e. a smaller cross section of the arc. This motion has the effect of increasing the value of the current density, however, since the amount of material involved in the calculation of the heat input is the same, the value of the arc current remains the same.

This method of finding the arc current will be much more accurate when some of the assumptions are removed. In particular, a good value for the arc lifetime must be found. More detail in this calculation is meaningless without the lifetime.

### 3. Pit depth experiment

The purpose of this experiment was to find if there is a relationship between a pit's depth and its diameter. To accomplish this copper films of thicknesses varying from one to ten microns were placed onto polished type 304 stainless steel targets. These targets were then illuminated with a single focused pulse of the CO<sub>2</sub> laser under roughly the same conditions.

Data was acquired using the scanning electron microscope. Its elemental analysis function was used to scan for sharp differences in element concentration over the pit. An example of a pit which did penetrate fully through the film is given in Figure 41, Figure 42 and Figure 43. An example which demonstrates a pit which did not fully penetrate is given by Figure 44 and Figure 45. The elemental analysis function will penetrate approximately one micron into the surface. This is not considered to be a significant source of error since it is changes in the elemental concentrations which are looked for. The fact that all analyzed pits either showed a sharp change in concentration or no apparent change at all further minimizes this as a source of error.

Figure 46 displays the results of this experiment. Raw data is provided in Appendix A. The data show that there is no correlation between pit depth and diameter for pitting on the copper films. This conclusion comes from the fact that in many cases pits with relatively smaller diameter penetrated the film whereas other much larger ones did not. This conclusion may be specific to pitting on copper films due to the sharp differences between the shapes of these pits and those previously investigated on uncoated stainless steel. There is also dramatic differences between the pits on the same target. Figure 41, Figure 44, Figure 47 and Figure 48 are just a few examples. The large range in error in the power densities in Appendix A is due to the measurements of the small area of the laser spot.

Figure 46 also shows that the maximum depth for pitting was less than 10 microns. No pit was found which fully penetrated the 9.88 micron film. This includes pits inside the laser spot. Difficulty in acquiring time on the SEM prevented further investigation.



Figure 41. Example pit which fully penetrated the copper film. (50S0X)

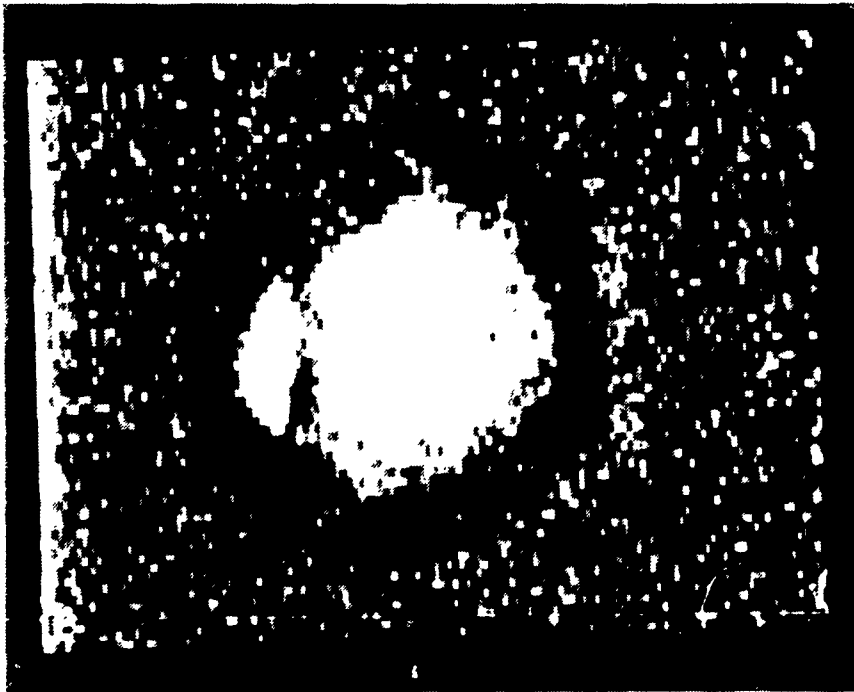


Figure 42. Iron distribution of Figure 41.

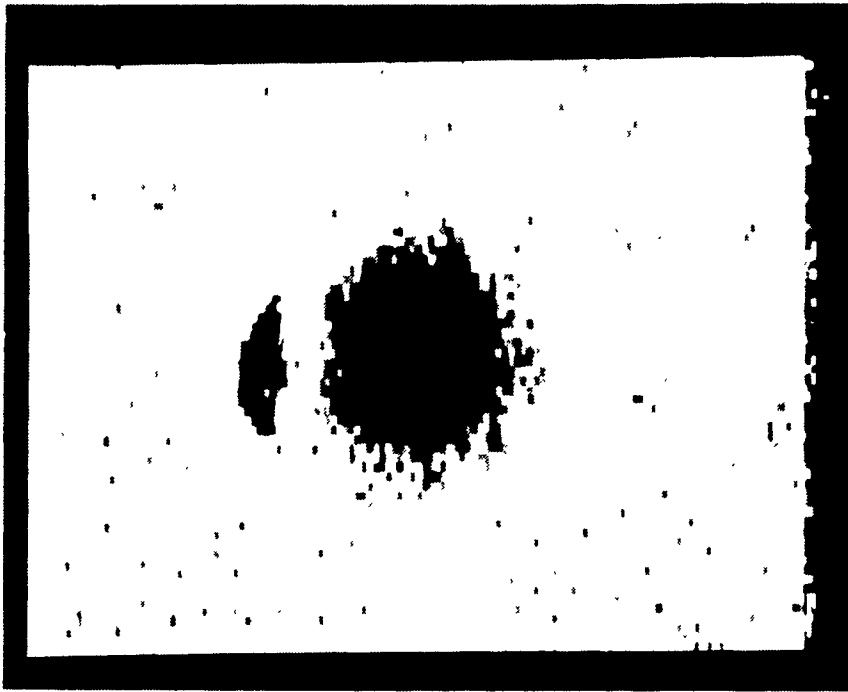


Figure 43. Copper distribution of Figure 41.

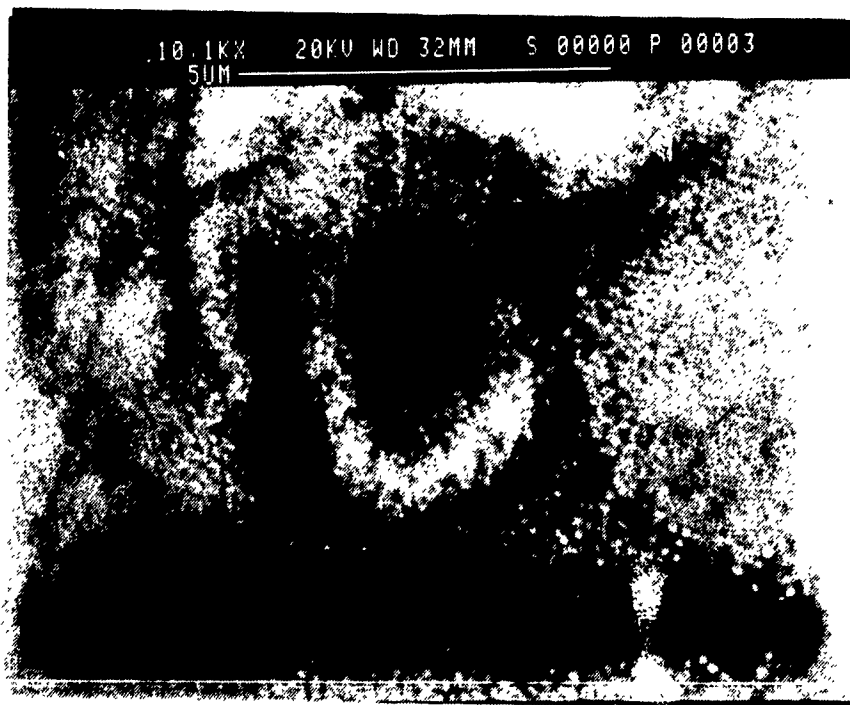


Figure 44. Example pit which does not penetrate the copper film.

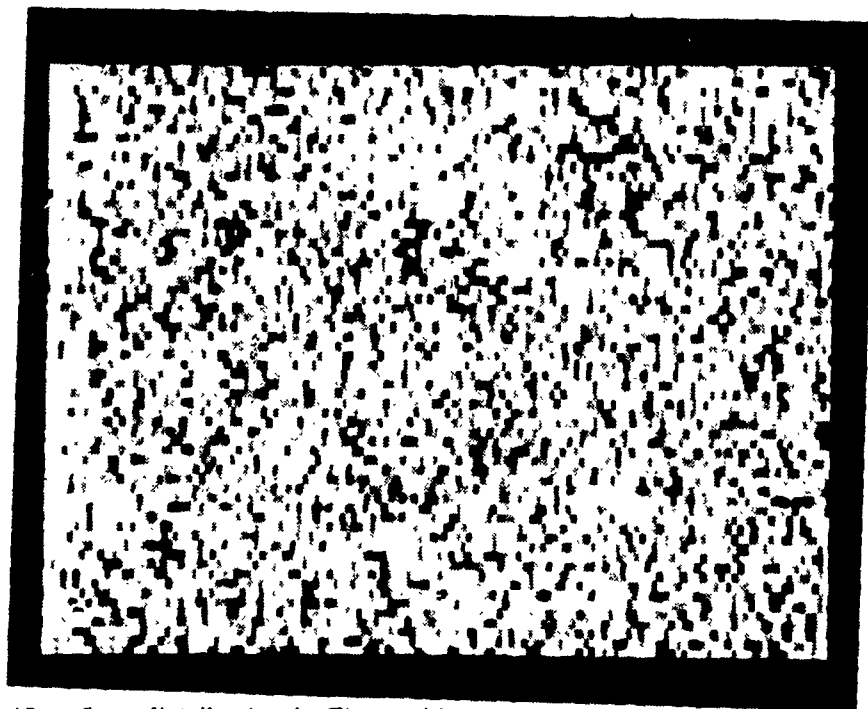


Figure 45. Iron distribution in Figure 44.

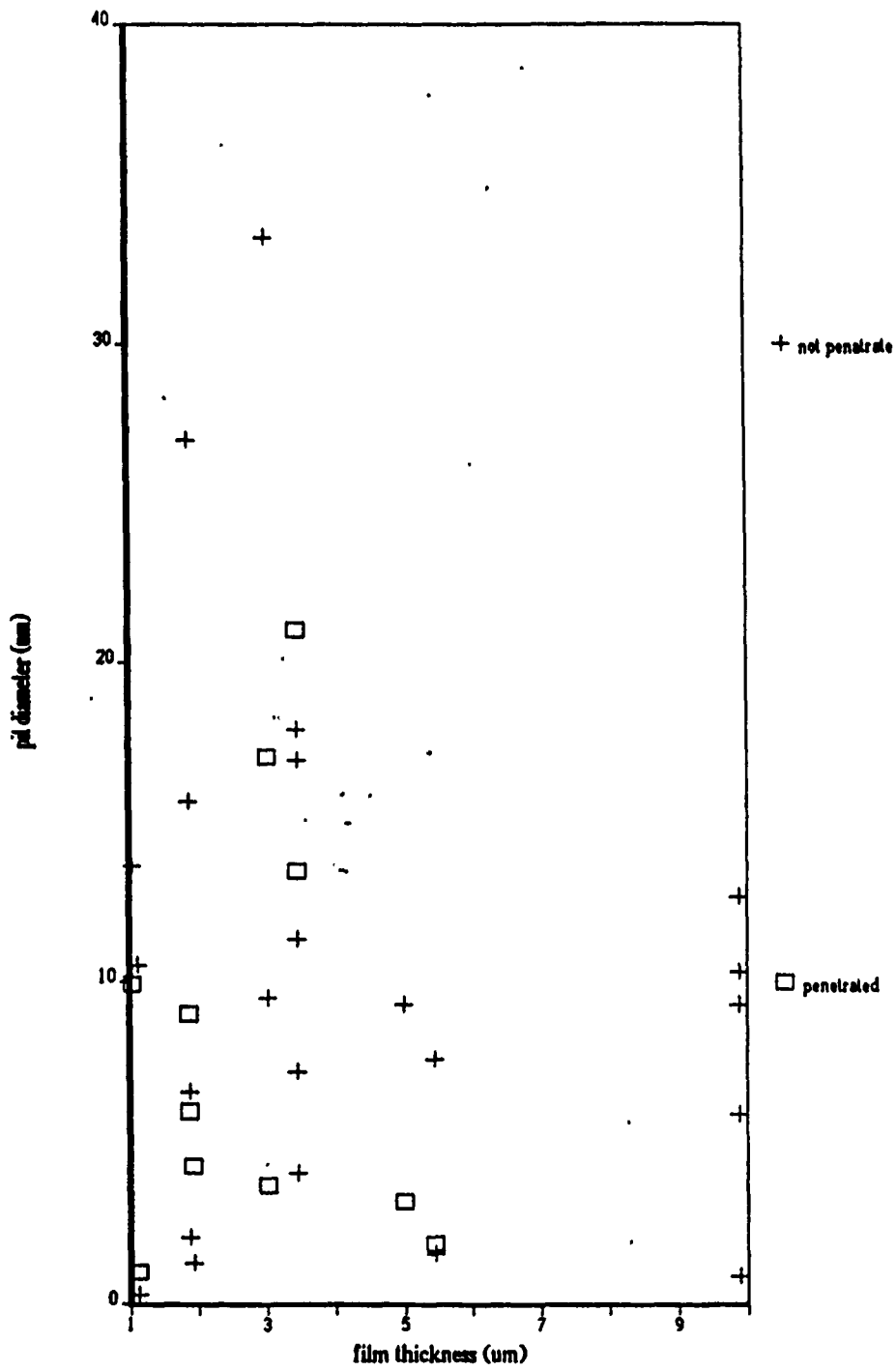


Figure 46. Results of pit depth versus pit diameter experiment.

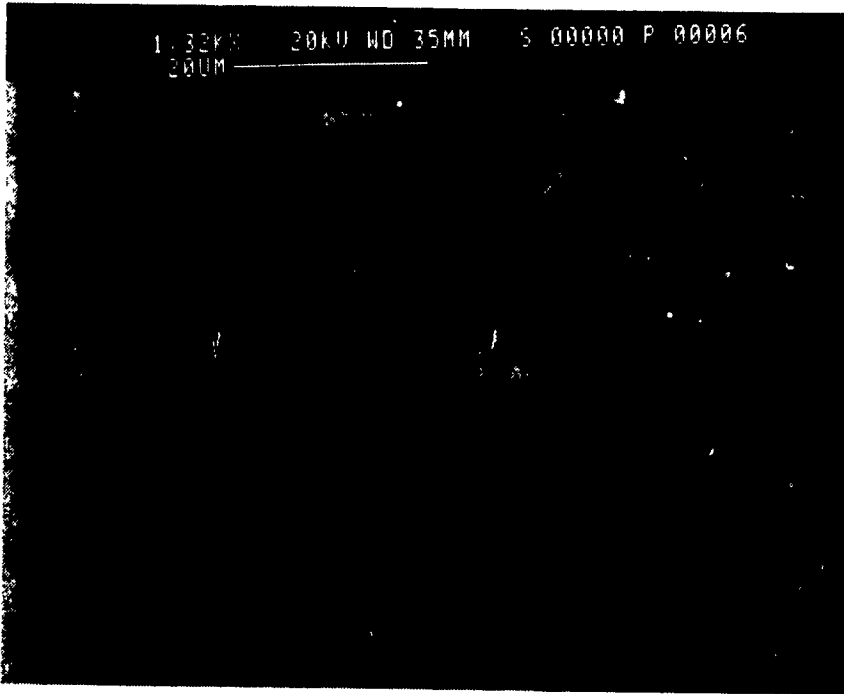


Figure 47. Example of Unipolar Arc pit diversity. (1320X)

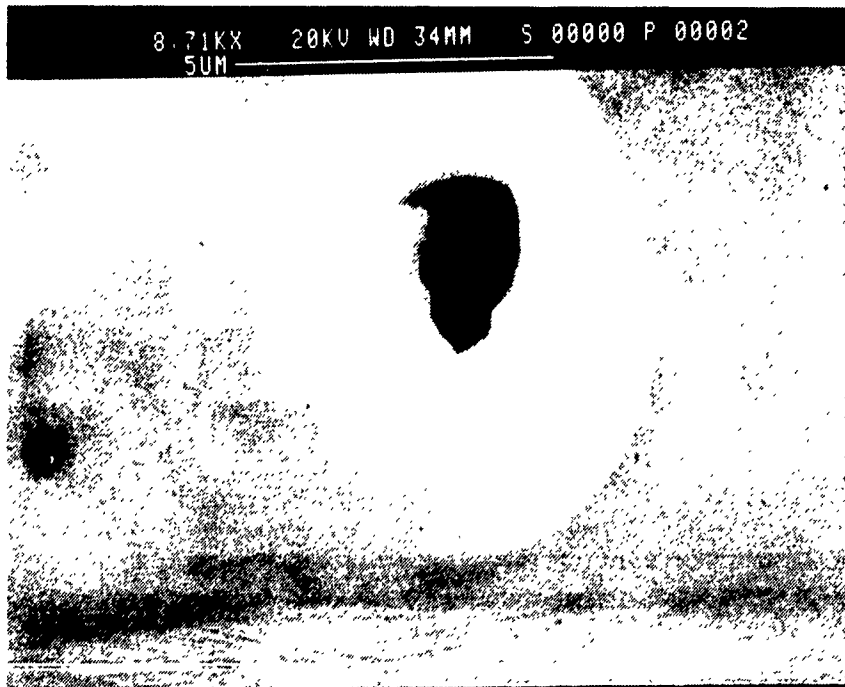


Figure 48. Example of Unipolar Arc pit diversity. (8710X)

## V. THE SURFACE DYNAMICS OF UNIPOLAR ARCING

The background theory combined with the experimental results provide an indication of the dynamics involved in the surface interaction. Simply put, the surface sees a high concentration of ions producing an intense electric field over a small region. This generates the emission of a high electron current which heats the surface producing melting and vaporization of material in that region. Indeed, this is quite similar to arc welding and so much of the physics of these two processes must be similar. This chapter will exploit that link. It begins with a theoretical description of the generation of the pit or keyhole as it is referred to in arc welding, and concludes with a theory on the formation of the rim. Much of the theory presented is specific to the macroscopic process of arc welding and is only qualitatively related to the microscopic process of unipolar arcing. Further research will be necessary to make it specific to unipolar arcing.

### A. PIT FORMATION

As mentioned in chapter II, the cathode spot is both emitting a high current of electrons and absorbing a large ion flux. Heat is mostly provided by the electron current with a small contribution from the energy of the ions (see Appendix B). The ion energy comes from their thermal energy, the energy gained in their acceleration through the cathode potential drop and their recombination energy. This recombination energy is approximately equal to the material's ionization energy. All this energy serves to heat the small region of the cathode spot. Heating of the cathode spot gives rise to melting, vaporization and thermal electron emission.

As described by Quigley [Ref. 15], in order for a pit to form the power density must be high enough for the combined effects of the ion pressure and the pressure caused by the vaporization of the material to produce a depression in the pool of molten liquid. Once formed the depth and shape of the pit will be determined by the forces involved, that is, the effects of those forces which tend to open the pit and those which tend to close it (see Figure 49).

#### 1. Forces which tend to open a pit

The forces which tend to open and maintain the pit are the ion pressure ( $p_i$ ), vapor pressure ( $p_v$ ) and the recoil pressure ( $p_r$ ). In the laser-target interaction the radiation pressure would also have to be considered, but this will be neglected here since the plasma-surface interaction is all that is being described.

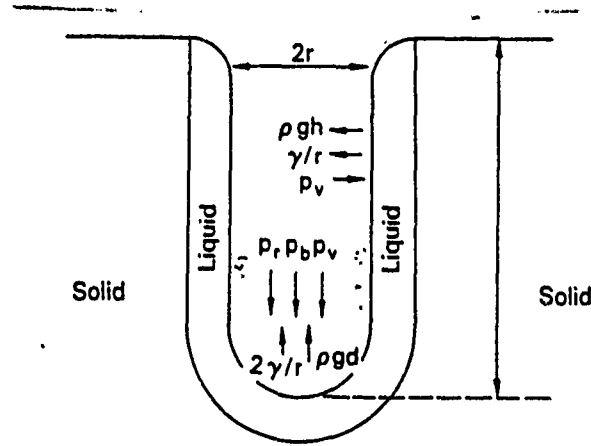


Figure 49. Forces involved in the formation of the pit. [Ref. 15, p.311]

The ion pressure comes from the momentum imparted to surface by the impact of the ions. It is given by

$$p_b = \frac{1}{2} \rho_i v^2 \quad \{49\}$$

where  $\rho_i$  is the ion density and  $v$  is their velocity. Schwirzke [Ref. 4] gives a plasma density of  $10^{16} \text{cm}^{-3}$  when one monolayer of atoms has been released from the surface. Schwirzke also stated an electron temperature of 18 eV. To find the upper limit on the beam pressure it is assumed that all of the ions enter into the sheath one debye length from the surface with negligible energy. The ions will be accelerated through the entire sheath potential. The velocity is then given by

$$v = \sqrt{\frac{2eV_f}{m_i}} \quad \{50\}$$

where  $m_i$  is the ion mass. With  $\rho_i = n_i m_i$ , the beam pressure becomes

$$\begin{aligned}
p_b &= \frac{1}{2} \rho_i v^2 \\
&= \frac{1}{2n_i} m_i \frac{2eV_f}{m_i} \\
&= n_i e V_f \\
&= 1.45 \times 10^5 \text{ N/m}^2.
\end{aligned}
\tag{51}$$

This is the upper bound on the beam pressure assuming a plasma density provided by the partial ionization of one monolayer of atoms. Currently the value of the plasma density above the pit during arcing is unknown.

The vapor pressure comes from the material vaporized inside of the pit. This pressure is dependent upon the temperature. Calculations of the temperature and thus the vapor pressure distribution inside of the pit are complicated due to the dynamic nature of that environment. The vapor pressures as a function of temperature for aluminum, copper and iron are given in Figure 50. Note the rapid decrease with temperature.

Lastly, the recoil pressure is due to the vapors leaving the surface with a finite velocity and hence imparting a recoil pressure onto the liquid surface. According to Quigley [Ref. 15, p.317] the recoil pressure is given by

$$p_r = \frac{W^2}{A^2 \rho_g Q^2}
\tag{52}$$

where  $W/A$  is the power density,  $\rho_g$  is the vapor density and  $Q$  is the energy required to vaporize one kilogram of the material. From the calculation of the arc current in chapter IV  $W/A$  is  $3.3 \times 10^{10} \text{ W/m}^2$  and  $Q$  is  $1.94 \times 10^6 \text{ J/kg}$ . The vapor density can be found by taking the mass of the vapor ejected and dividing by its volume. Assuming that the surface temperature is 2200 K, then the velocity of the vapors is 930 m/s. If the arc lasts for one microsecond the vapors will travel  $9.3 \times 10^{-4} \text{ m}$ . Taking data from the pit used for the arc current calculation in chapter IV finds a vapor density of  $4.49 \text{ kg/m}^3$ . The recoil pressure is then

$$p_r = 6.44 \times 10^7 \text{ N/m}^2.
\tag{53}$$

The values presented here are only rough estimations accurate to only an order of magnitude. Nonetheless, it is clear that the recoil pressure is a significant force tending to create the pit in the liquified surface. The contribution of the ions depends

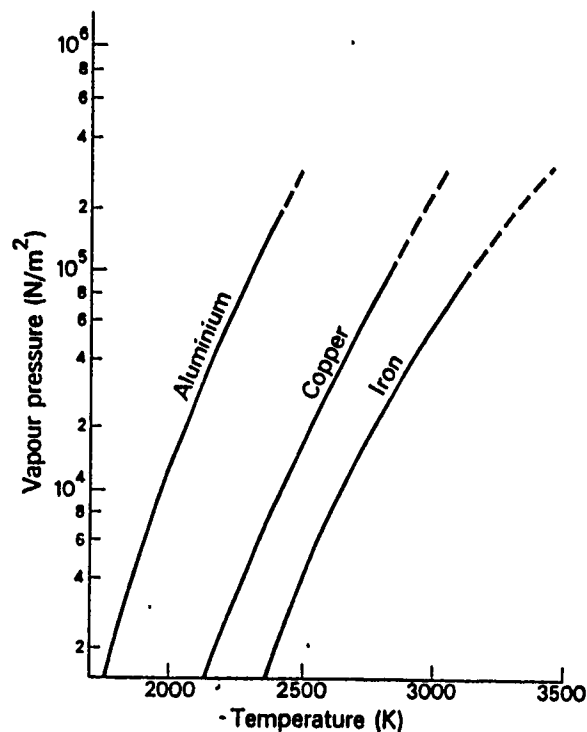


Figure 50. Vapor pressure versus temperature for Aluminum, Copper and Iron. [Ref. 15, p.32].

on their density. The ion density would have to be two orders of magnitude higher for the ion pressure to become comparable with the recoil pressure.

## 2. Forces which tend to close a pit

The forces which will act to close a pit are gravity and surface tension. The gravitational pressure,  $\rho gh$ , at any point is simply equal to the weight of the metal above it. In Figure 49  $h$  is the depth at any particular point in the pit, and  $d$  is the maximum pit depth. This force should not be significant in pits formed by unipolar arcing.

Surface tension can be thought of as the force which acts to minimize the surface area of a liquid. In the case of pitting the surface tension force acts against the ion, vapor and recoil pressure forces as shown in Figure 49. Assuming that the surface at the bottom of the pit is a hemisphere, then the surface tension pressure is

$$p_y = \frac{2\gamma}{r} \quad \{54\}$$

where  $\gamma$  is the surface tension coefficient and  $r$  is the radius of the hemisphere. The surface tension coefficient for copper varies from 1.03 to 1.15 N/m depending on the temperature (see Figure 51). Assuming a value of 1.1 N/m and a pit radius of one micron gives a surface tension pressure of

$$p_y = 2.2 \times 10^6 \text{ N/m}^2. \quad \{55\}$$

While this value is much greater than either the ion pressure or the vapor pressure, it is much less than the recoil pressure.

### 3. Overview of the dynamics of pit formation

The process of pit formation begins with the concentration of an electric field around a 'whisker.' This causes increased ion bombardment of the whisker, heating it and increasing the emission of adsorbed gases and other neutral particles. Collisions with electrons ionize a small percentage (approximately 2%) of these neutrals which causes a dramatic rise over the background plasma density (about 4000X) above the whisker [Ref. 4]. This rise in plasma density rapidly reduces the debye length with a subsequent increase in the electric field above the surface. When the electric field becomes high enough arcing occurs. This is followed by a rapid temperature rise in the cathode spot accompanied by melting and vaporization of the surface. This vaporization creates a recoil pressure which overcomes the surface tension pressure and pushes a pit into the surface. As long as the plasma density above the cathode spot remains high the pit will deepen. Since it is the high electron temperature along with the high local neutral concentration which generates the high local plasma density, the plasma density in the pit will decrease with pit depth. This is due to the plasma in the pit becoming isolated from the bulk plasma. When the electron concentration and energy in the pit become sufficiently depleted such that ionization of neutrals is significantly reduced, then the plasma density will drop. The subsequent reduction in the debye length lowers the electric field past the point where arcing stops.

Andrews and Atthey [Ref. 17] give an excellent mathematical description of the generation of a pit, or 'keyhole,' by a continuous high power laser beam. Their pit is, however, on the order of a millimeter in diameter and the heat input is from the laser as it drills the hole. Further research may be able to modify their solution to fit the physics of unipolar arcing. Their solutions to the hole profiles for different power den-

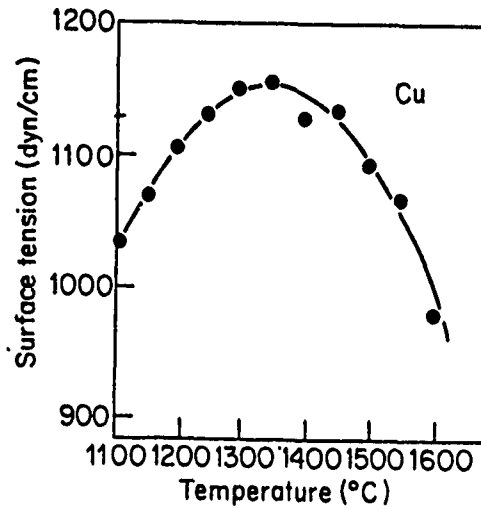


Figure 51. Surface tension coefficient versus temperature for copper. [Ref. 16]

sities is shown in Figure 52. In this graph 'a' represents the beam radius. Plots A through E represent increasing power density.

#### B. RIM FORMATION

Two forces are responsible for the formation of the rim: the ejection of the vapor from the pit and surface tension. The vapor ejection serves to remove the liquid on the sides of the pit and pushes it radially outwards as it exits from the pit. The motion of the molten rim away from the pit will be shown to most likely be due to a gradient in the surface tension.

##### 1. Dynamics due to the ejected vapor

The vapor produced in the pit exerts forces on the walls of the pit as shown in Figure 49. The rushing vapor produces a shear stress along the wall of the pit. Since that wall is a liquid-vapor interface the shear stress and the pressure gradient produce vertical flow which brings the liquid out of the pit.<sup>1</sup> At the exit of the pit the radial vapor pressure gradient pushes the liquid radially outwards to form a small rim around the pit.

<sup>1</sup> The liquid is also removed from the pit by the action of the recoil pressure displacing molten metal in the pit center.

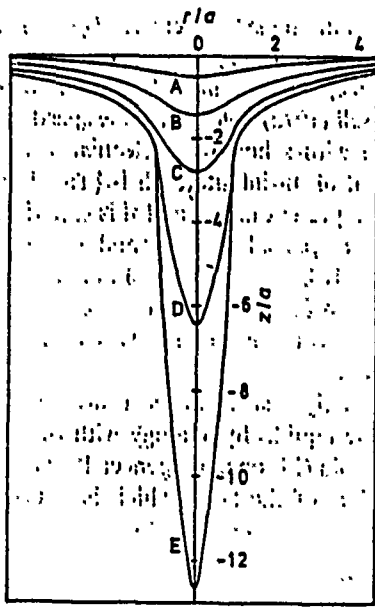


**Figure 52.** Example pit profiles.: equilibrium hole profiles calculated to be produced by a continuous high power laser beam whose diameter is on the order of a millimeter.[Ref. 17]

The vertical flow also transports heat. This heat transport acts to produce more melting on the surface which explains the downward slope found between the rim and the pit (Figure 53 and Figure 54).

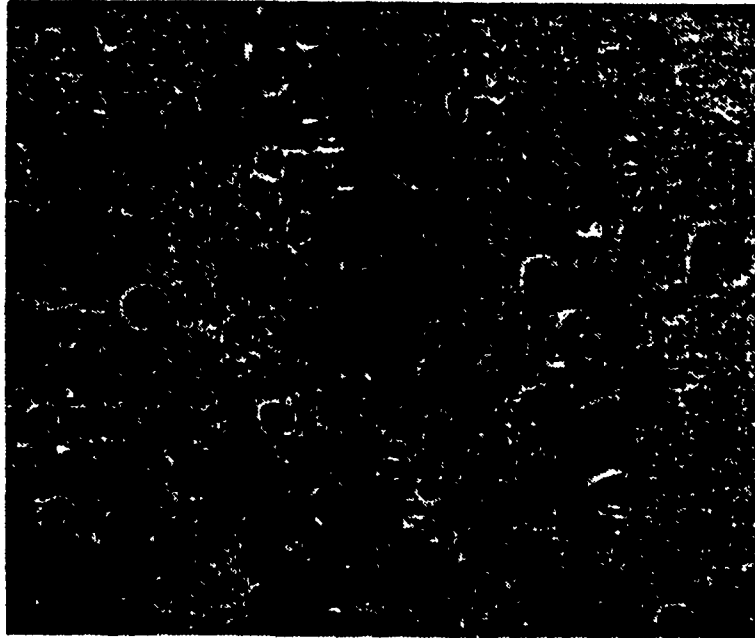


Figure 53. Unipolar arc craters on stainless steel target: (700X with SEM)[Ref. 18] ( — 10 $\mu$ m).



Figure 54. Unipolar arc craters on stainless steel target: (cathode holes are approximately 0.7 micron diameter) [Ref. 18].

## 2. Dynamics due to surface tension

Surface tension also acts to transport the surface liquid radially away from the region of the pit. How it does this depends upon whether or not the pit fully penetrated the material, in this case the copper film. If the pit fully penetrates it will be shown that the surface tension acts to reduce the surface area. In so doing the rim expands radially until the heat contained in the liquid is no longer sufficient to liquify more of the copper film. Two arguments will be given for the case where the arc does not fully penetrate the material of the film. The argument by Lancaster [Ref. 15, p.113] shows that when the surface tension decreases with temperature it will induce an outward radial flow on the surface of the liquid. Unfortunately, typographical errors in the reference produced a break in his argument. Attempts to resolve this produce an argument from which outward radial flow is produced by a surface tension which increases with temperature. Both arguments will be given concurrently.

### a. Full film penetration

Since the pit depth is generally on the order of a few microns, then a film of that thickness or less on a surface will be easily penetrated by a unipolar arc. When this occurs the surface tension of the liquid acts to reduce its surface area. It will have a semicircular cross section and have a contact angle,  $\theta$ , with the underlying surface (Figure 55). This contact angle is given by

$$\cos \theta = \frac{\gamma_B - \gamma_{AB}}{\gamma_A} \quad \{56\}$$

where  $\gamma_B$ ,  $\gamma_A$  and  $\gamma_{AB}$  are the surface tensions of the underlying solid surface, the liquid film and the surface-liquid interface respectively (Figure 56).

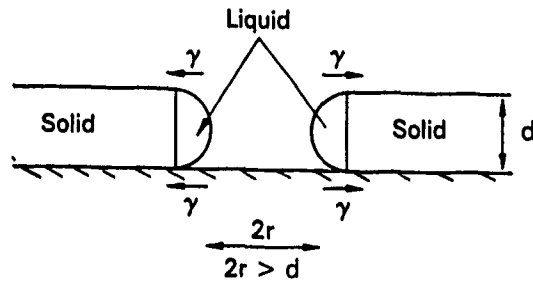


Figure 55. Pit fully penetrating a film over a surface.

The surface tension produces an outward radial force on the film surface (Figure 55). As heat is transferred from the liquid to the solid film more of the solid film will undergo the transition to liquid and the 'rim' will progress radially away from its starting point. This will continue until there is no longer sufficient heat present for the transition to continue. At this point the heat will continue to flow out of the liquid and it will solidify in place while maintaining its shape.

While this explains the damage found in Figure 39 it does not completely explain that found in Figure 38. The large size of this damage indicates that it could not have been caused by a single arc in a small area. Thus either several arcs produced this damage or the arc followed the rim as it receded. The mechanism for the arc following the receding rim may come from the reduced vaporization temperature for copper in a vacuum. The melting point for copper is 1083 °C. Depending on the vapor pressure, its boiling point can be very near its melting point. At a pressure of  $7.6 \times 10^{-4}$  mmHg the boiling point is 1118 °C. The melting point for the iron in the stainless steel is 1535 °C. Thus the inner corner of the copper rim could have become the source of the vapors producing the plasma density needed for arcing. Thus the arc following the rim as it recedes may have been the heat source which generated the damage.

*b. Flow induced by a surface tension gradient*

The following argument deals with steady flow conditions in a weld pool. While the process of unipolar arcing is on a much smaller scale and is inherently dy-

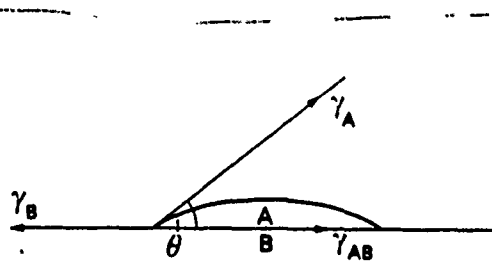


Figure 56. Surface tension forces on a liquid drop in contact with a surface. [Ref. 15, p.35]

namic much of the same physics should be occurring. Thus this argument is not meant to present a full description of a mechanism for liquid flow during unipolar arcing, rather it is only to present a 'possible' mechanism for this flow. More research is necessary to determine the validity of this argument in relation to the unipolar arc. Most of the following argument comes directly from Ref. 15.

The general solution for flow generated in a conducting fluid by an electric current which diverges from a point source on the surface (Figure 57) was found by Lundquist [Ref. 19]. Lancaster [Ref. 15, p.113] applied this to a point source at the origin entering a semi-infinite liquid whose surface is on the plane  $\theta = \pi/2$ . The stream function, in spherical coordinates, for this case is given by

$$\Psi(r,\lambda) = \frac{\mu_o I^2 r}{4\pi^2 \eta} [a\lambda^2 + b\lambda + c + (1+\lambda) \ln(1+\lambda)] \quad \{57\}$$

where  $\mu_o$  = magnetic permeability

I = electric current

$\eta$  = viscosity

$\lambda = \cos \theta$

and a, b and c are constants. The boundary conditions for this problem require that

$$\Psi(r,0) = 0 \quad \{59\}$$

$$\Psi(r, \lambda) = 0. \quad \{60\}$$

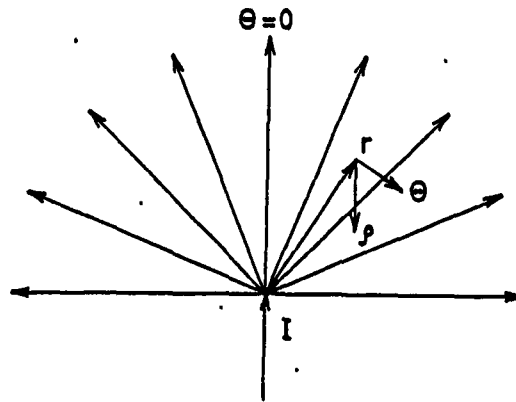


Figure .57. The current  $I$  enters at the origin of the coordinate system and flows radially into a conducting fluid. [Ref. 19, p. 90]

When the system is in steady state the net shear stress at the surface must be zero. Hence there is a balance between the stress due to the flow,  $p_{r\theta}$ , and that due to the surface tension. Thus

$$\left[ p_{r\theta} + \frac{\partial \gamma}{\partial r} \right]_{\lambda=0} = 0. \quad \{61\}$$

Lancaster then solves for the shear stress with the result that

$$p_{r\theta} = \frac{\mu_0 I^2}{4\pi^2 r^2} \left\{ \frac{2}{\sqrt{1-\lambda^2}} \sqrt{a\lambda^2 + b\lambda + (1+\lambda) \ln(1+\lambda) - (1-\lambda^2)} \left[ 2a + \frac{1}{1+\lambda} \right] \right\}. \quad \{62\}$$

Attempts to reproduce this result have failed. Calculations shown in Appendix C show the shear stress to be given by

$$p_{r\theta} = \frac{\mu_0 I^2}{4\pi^2 r^2} \left\{ \frac{2}{\sqrt{1-\lambda^2}} [a\lambda^2 + b\lambda + (1+\lambda) \ln(1+\lambda)] + \sqrt{1-\lambda^2} \left( 2a + \frac{1}{1+\lambda} \right) \right\}. \quad \{63\}$$

The difference lies in the numerator term under the square root sign in equation (61). Equation (62) shows that only the  $1-\lambda^2$  term in the numerator is under the square root. This is also the only term multiplied with the  $2a+1/1+\lambda$ , and the sign in front of the

$\sqrt{1-\lambda^2}$  is plus in equation (62) while in equation (61) it is minus. It is most likely that typographical errors are the cause of much of the problem since for  $\lambda = 0$  equation (61) yields a complex value. However, when Lancaster combines equation (60) with equation (61) he gets

$$-\frac{\mu_0 I^2}{4\pi^2 r^2} (2a+1) + \frac{\partial \gamma}{\partial r} = 0 \quad \{64\}$$

so that

$$a_L = \frac{1}{2} \left[ \frac{4\pi^2 r^2 \frac{\partial \gamma}{\partial r}}{\mu_0 I^2} - 1 \right]. \quad \{65\}$$

Similarly, combining equation (60) with equation (62) gives

$$a_D = -\frac{1}{2} \left[ \frac{4\pi^2 r^2 \frac{\partial \gamma}{\partial r}}{\mu_0 I^2} + 1 \right] \quad \{66\}$$

where the subscripts L and D will refer to the different values found by Lancaster and Downs respectively.

The first boundary condition requires that  $c=0$ , the second requires that  $b = -a - 2 \ln 2$ . The respective stream functions then become

$$\Psi_L = \frac{\mu_0 I^2 r}{4\pi^2 \eta} \left[ \frac{1}{2} \left( \frac{4\pi r^2 \frac{\partial \gamma}{\partial r}}{\mu_0 I^2} - 1 \right) \lambda^2 - \frac{1}{2} \left( \frac{4\pi r^2 \frac{\partial \gamma}{\partial r}}{\mu_0 I^2} - 1 - 4 \ln 2 \right) \lambda \right. \\ \left. + (1+\lambda) \ln(1+\lambda) \right] \quad \{67\}$$

$$\Psi_D = \frac{\mu_0 I^2 r}{4\pi^2 \eta} \left[ -\frac{1}{2} \left( \frac{4\pi r^2 \frac{\partial \gamma}{\partial r}}{\mu_0 I^2} + 1 \right) \lambda^2 + \frac{1}{2} \left( \frac{4\pi r^2 \frac{\partial \gamma}{\partial r}}{\mu_0 I^2} + 1 - 4 \ln 2 \right) \lambda \right. \\ \left. + (1+\lambda) \ln(1+\lambda) \right]. \quad \{68\}$$

In spherical polar coordinates the radial velocity is given by

$$V_r = \frac{1}{r^2 \sin \theta} \frac{\partial \Psi}{\partial \theta} = -\frac{1}{r^2} \frac{\partial \Psi}{\partial \lambda} \quad \{69\}$$

so that the velocities at the surface are

$$[V_{rL}]_{\lambda=0} = -\frac{\mu_o I^2}{4\pi^2 \eta r} \left( \frac{3}{2} - 2 \ln 2 - \frac{2\pi^2 r^2}{\mu_o I^2} \frac{\partial \gamma}{\partial r} \right) \quad \{70\}$$

$$[V_{rD}]_{\lambda=0} = -\frac{\mu_o I^2}{4\pi^2 \eta r} \left( \frac{3}{2} - 2 \ln 2 + \frac{2\pi^2 r^2}{\mu_o I^2} \frac{\partial \gamma}{\partial r} \right). \quad \{71\}$$

In the absence of a surface tension gradient both cases yield a radial velocity given by

$$[V_r]_{\lambda=0} = -\frac{\mu_o I^2}{4\pi^2 \eta r} \left( \frac{3}{2} - 2 \ln 2 \right) \quad \{72\}$$

and the flow induced by the current is radially inwards on the surface. The physical significance between these arguments comes when there is a gradient in the surface tension over the surface. Lancaster finds that the flow is reversed, i.e. flow is radially outwards, if the gradient in surface tension is finite and positive such that

$$\frac{2\pi^2 r^2}{\mu_o I^2} \frac{\partial \gamma}{\partial r} > 0.1137 = \frac{3}{2} - 2 \ln 2. \quad \{73\}$$

Calculations shown thus far reveal that flow will be reversed only if the gradient in surface tension is finite and negative such that

$$\frac{2\pi^2 r^2}{\mu_o I^2} \frac{\partial \gamma}{\partial r} < -0.1137. \quad \{74\}$$

Given a point source of heat at the source where  $Q_s$  is the power of the source,  $C_p$  the specific heat and  $\rho$  the density, then the temperature distribution [Ref. 15] is

$$T = \frac{Q_s}{4\pi\rho C_p \alpha r} \quad \{75\}$$

where  $\alpha$  is the thermal diffusivity. The temperature gradient is then

$$\frac{dT}{dr} = -\frac{Q_s}{4\pi\rho C_p \alpha r^2} \quad \{76\}$$

If V is the power in volts, then  $Q_s = VI$  and with

$$\frac{\partial\gamma}{\partial r} = \frac{\partial\gamma}{\partial T} \frac{dT}{dr} \quad \{77\}$$

then

$$\frac{2\pi^2 r^2 \frac{\partial\gamma}{\partial r}}{\mu_o I^2} = -\frac{\pi V \frac{\partial\gamma}{\partial T}}{2\rho C_p \alpha \mu_o I} \quad \{78\}$$

Lancaster's requirement for outward radial flow then becomes

$$\frac{\pi V \frac{\partial\gamma}{\partial T}}{2\rho C_p \alpha \mu_o I} < -0.1137 \quad \{79\}$$

whereas calculations show the requirement to be

$$\frac{\pi V \frac{\partial\gamma}{\partial T}}{2\rho C_p \alpha \mu_o I} > 0.1137. \quad \{80\}$$

The surface tension for most pure elements decreases with increasing temperature, however small amounts of surface active elements such as oxygen and sulphur significantly reduce the surface tension (Figure 58 and Figure 59). As a function of temperature, high enough concentrations can lead to an increasing surface tension with temperature. Also, the change in surface tension with temperature of copper is positive at lower temperatures and negative at higher temperatures as shown in Figure 51. Thus either solution may generate outward radial flow.

Lancaster also uses figures from an article by Matsunawa [Ref. 20] (Figure 60 and Figure 61 to prove his case. However, if Matsunawa is following the sign convention for flow in terms of a change in the stream function (Figure 62 on page 73) then Figure 60 and Figure 61 prove just the opposite.

c:/figref ref/figref page = no ref/\*\*

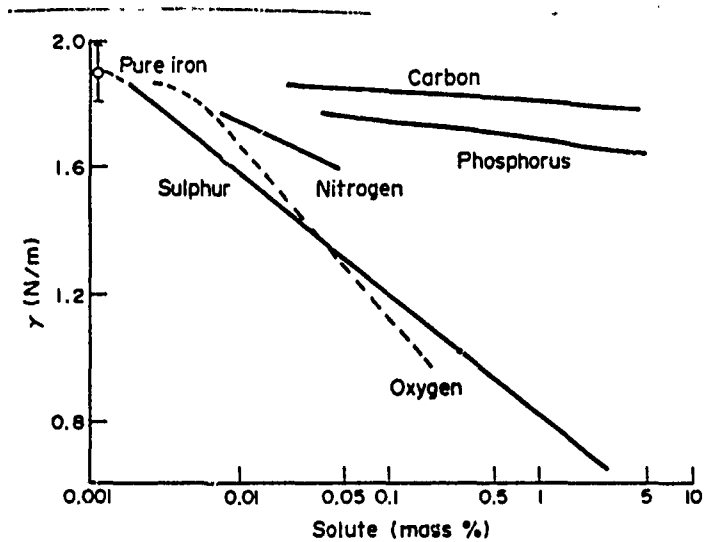


Figure 58. Effect on the surface tension of iron by various non-metallic elements. [Ref. 15, p.39]

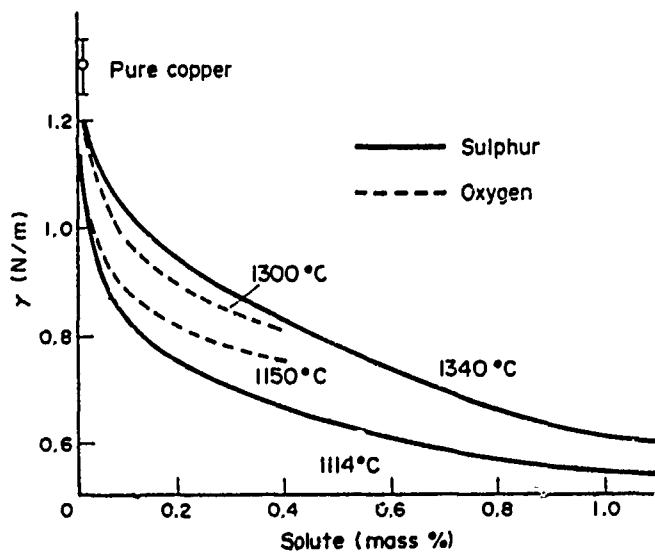


Figure 59. Effect on the surface tension of copper by oxygen and sulphur. [Ref. 15, p.39]

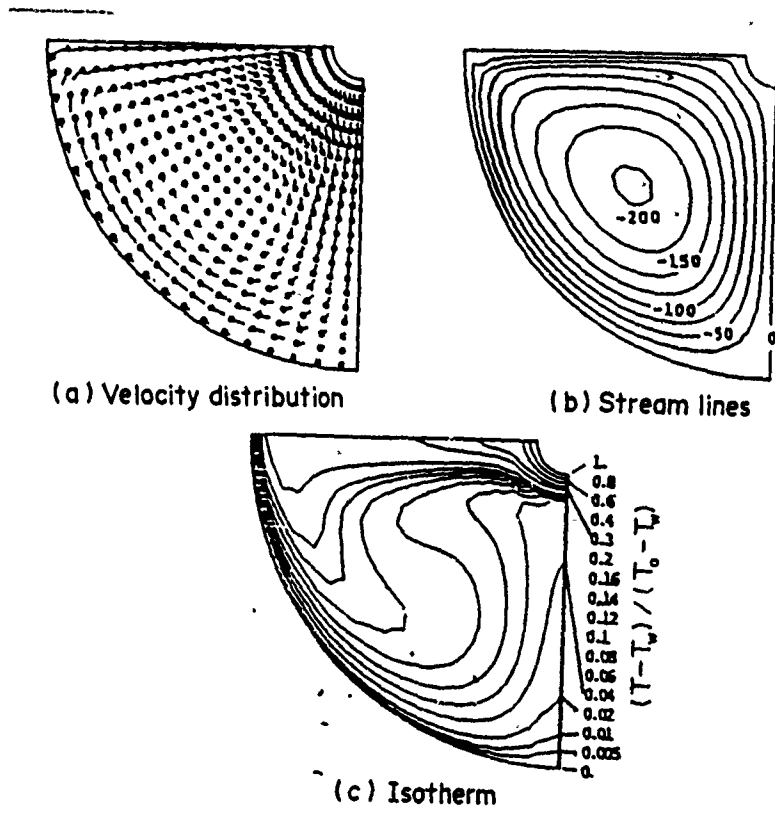


Figure 60. The velocity distribution, streamlines and isotherms: Marangoni flow with a negative gradient of surface tension with temperature [Ref. 15, p.117].

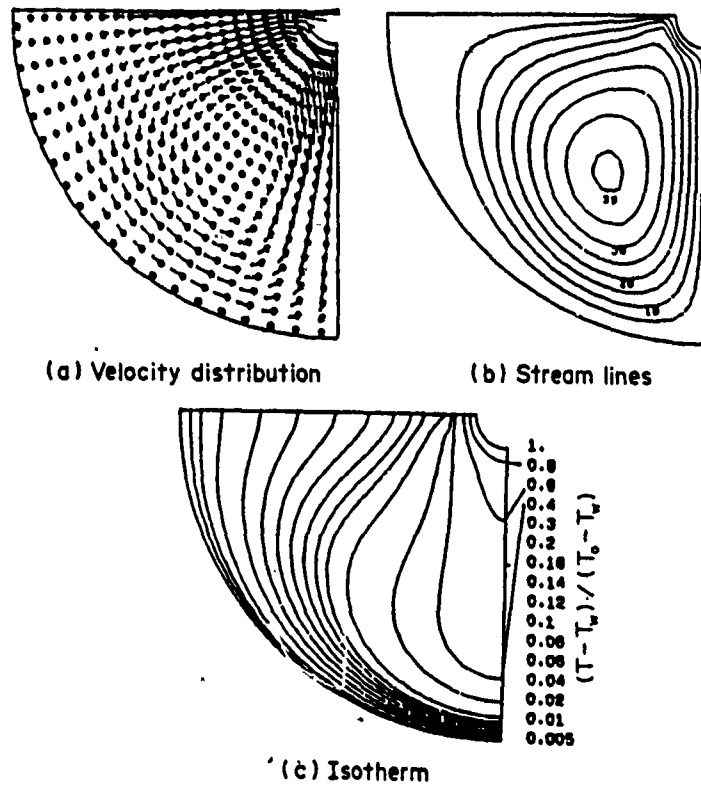


Figure 61. The velocity distribution, streamlines and isotherms: Marangoni flow with a positive gradient of surface tension with temperature [Ref. 15, p.118].

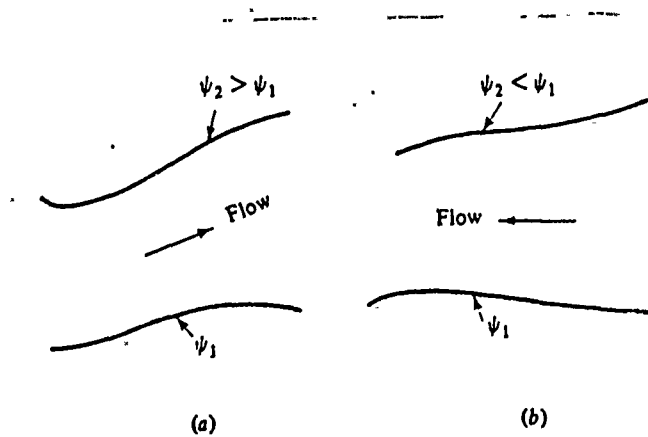


Figure 62. Sign-convention for flow in terms of a change in the stream function. [Ref. 21, p.224]

## VI. CONCLUSIONS

This research has provided a broad overview of the dynamics of unipolar arcing on the surface. It was shown that a significant amount of material is ejected during arcing, the bulk of which is ejected normal to the surface. This being independent of the incidence angle of the laser implies that it is the plasma produced by the laser pulse that caused the target damage. Ring structures found when the ejected material deposits on another surface indicates that the arcing oscillates and/or has a more complex structure than previously considered. Experiments also revealed no apparent connection between pit depth and diameter for the copper films.

Experiments using thin films imply that damage increases as melting and boiling points decrease, however, this has not been rigorously shown. Other parameters may have significant contributions as well. The role of surface tension during arcs which fully penetrate the film is clear. By reducing the surface area it produces a rim which expands radially. Radial expansion will continue so long as the molten metal contains sufficient heat to liquify the adjacent film.

In investigating the role of surface tension an apparent similarity between unipolar arcing and arc welding was discovered. Exploiting this similarity has revealed a possible explanation of the dynamics of pit formation. The primary force generating the pit appears to be the recoil pressure caused by the evaporating surface. This acts against the surface tension of the molten liquid to push a pit in the metal. Molten metal is removed from the walls of the pit by the action of the vapors as they rush out. The rim appears to be formed by the combined forces of the expanding gases (as they leave the pit) and radial motion caused by a gradient in the surface tension. It must be emphasized that this theory is only preliminary. There are many differences between unipolar arcing and arc welding. These may invalidate much of this theory.

Clearly, further research into the surface dynamics is required. The fruits of this research will provide better choices of materials for Tokamaks, spacecraft and any other devices which will come into contact with a plasma. Specifically, the following areas need to be further investigated:

- how a material's melting and boiling points affect damage and what role its conductivity plays;
- the cause(s) of the ring deposition patterns;

- many of the assumptions need to be removed and the theory made specific to Unipolar Arcing.

**APPENDIX A. RAW DATA FROM PIT DEPTH VERSUS DIAMETER  
EXPERIMENTS**

**Table 2. DATA FOR PITS WHICH DID NOT  
PENETRATE THE COPPER FILM.**

film thick- ness ( $\mu\text{m}$ )	pit diam- eter ( $\mu\text{m}$ )	vacuum ( $10^{-5}$ mmHg)	laser pulse energy (J)
1.13	$0.3 \pm 0.1$	3.2	-----
1.89	$1.3 \pm 0.2$	2.4	15.0
1.89	$3.4 \pm 0.5$	2.4	15.0
3.03	$17.9 \pm 1.5$	2.3	11.7
3.03	$7.2 \pm 0.2$	2.3	11.7
3.03	$16.9 \pm 1.5$	2.3	11.7
3.03	$1.6 \pm 0.5$	2.3	11.7
3.03	$0.9 \pm 0.3$	2.3	11.7
5.0	$12.6 \pm 0.5$	2.3	11.9
5.0	$9.3 \pm 1.2$	2.3	11.9
5.0	$10.3 \pm 1.4$	2.3	11.9
5.0	$5.9 \pm 0.4$	2.3	11.9
5.45	$7.6 \pm 0.3$	2.3	15.8
9.88	$13.6 \pm 0.5$	2.0	15.7
9.88	$9.5 \pm 1.0$	2.0	15.7
9.88	$33.3 \pm 5.0$	2.0	15.7
9.88	$9.3 \pm 0.5$	2.0	15.7
9.88	$10.5 \pm 1.5$	2.3	12.1
9.88	$15.6 \pm 1.0$	2.3	12.1
9.88	$27.0 \pm 2.0$	2.3	12.1

**Table 3. DATA FOR PITS WHICH PENETRATED THE COPPER FILM.**

film thickness ( $\mu\text{m}$ )	pit diameter ( $\mu\text{m}$ )	vacuum ( $10^{-5}$ mmHg)	laser pulse energy (J)
1.05	$9.9 \pm 1.7$	2.4	12.2
1.13	$1.0 \pm 0.2$	3.2	----
1.89	$5.5 \pm 0.5$	2.4	15.0
1.89	$9.0 \pm 0.5$	2.4	15.0
1.94	$4.3 \pm 0.3$	2.3	15.0
3.03	$17.0 \pm 3.0$	2.3	11.7
3.03	$3.7 \pm 1.0$	2.3	11.7
3.47	$13.4 \pm 0.7$	2.4	15.8
5.0	$3.2 \pm 0.5$	2.3	11.9
5.45	$1.9 \pm 0.5$	2.3	15.8

## APPENDIX B. ION ENERGY CONTRIBUTION

The purpose of this appendix is to provide some good estimates of the energy contributed by the ions. The ions will contribute the energy they release as they combine with one of the surface electrons (hereafter referred to as recombination energy) and the kinetic energy they acquire as they traverse the sheath. It will be shown that the recombination energy is insignificant, whereas the kinetic energy is significant. For simplicity, throughout the following arguments it will be assumed that only the latent heat of vaporization is needed to vaporize the material. The ions must be able to provide this amount of energy if they are to reproduce their numbers.

### A. RECOMBINATION ENERGY CONTRIBUTION

Kittel [Ref. 22, p.53] defines the cohesive energy,  $E_c$ , as "the energy that must be added to the crystal to separate its components into neutral free atoms at rest, at infinite separation, with the same electronic configuration." For the purposes of the following argument the cohesive energy will be assumed to be the energy needed to vaporize the crystal. For copper this energy is

$$E_c = 3.49 \text{ eV/atom.} \quad \{81\}$$

The recombination energy provided by the ions will be approximately equal to the material's ionization energy. For copper the recombination energy,  $E_i$ , is then

$$E_i = 7.72 \text{ eV/ion.} \quad \{82\}$$

Thus the fraction of neutrals released that must be ionized so that the same number of neutrals can be vaporized by the recombination energy alone is

$$\frac{E_c}{E_i} = \frac{3.49 \text{ eV/atom}}{7.72 \text{ eV/ion}} = 0.45 \text{ ions, atom} \quad \{83\}$$

which is quite high.

Since the majority of the ions (generated from the ejected neutrals) which return to the pit surface are produced in the sheath, then for simplicity it will be assumed that all of those ions are produced in the sheath. The number of neutrals which are ionized in the sheath is proportional to the ratio of the debye length,  $\lambda_D$ , and the electron mean free

path,  $\lambda_e$ . The debye length was defined in chapter II, the electron mean free path is given by

$$\lambda_e = \frac{1}{n_o \sigma_i} \quad \{84\}$$

where  $n_o$  is the neutral particle density and  $\sigma_i$  is their ionization cross section ( $\approx 10^{-21} \text{m}^2$ ). Given that each monolayer of atoms vaporized must undergo enough ionizations such that the ions produced deliver sufficient energy to the cathode surface to release another monolayer of atoms, then the neutral particle density can be taken to be

$$n_o = \frac{\rho_p}{\lambda_D} \quad \{85\}$$

where  $\rho_p$  is the particle density of one monolayer of the surface ( $\approx 2.16 \times 10^{19} / \text{m}^2$  for copper). The fraction of neutrals which become ionized in the sheath is then

$$\begin{aligned} \frac{n_i}{n_o} &= \frac{\lambda_D}{\lambda_e} \\ &= \lambda_D n_o \sigma_i \\ &= \lambda_D \left( \frac{\rho_p}{\lambda_D} \right) \sigma_i \\ &= \rho_p \sigma_i \\ &\approx .022. \end{aligned} \quad \{86\}$$

Thus recombination only provides  $.022 \cdot .45 = .049 = 4.9\%$  of the energy needed. This does not take into account the ionizations produced by the electron current. This would entail a significant complication to this calculation and must be left for further study.

## B. KINETIC ENERGY CONTRIBUTION

To find the maximum possible contribution of the kinetic energy it is assumed that the ions which go to the surface are produced one debye length from the surface. Schwirzke [Ref. 4] found that the vast majority of the ions generating the short debye length (and thus Unipolar Arcing) come from neutrals ejected from the surface. Thus it will be assumed that all of the ions are produced from neutrals evaporated from the surface. The kinetic energy that they provide upon striking the surface is then

$$KE = \frac{1}{2} mv^2. \quad \{87\}$$

If the initial velocity is assumed to be negligible, then the ion velocity is given by

$$v = at \quad \{88\}$$

where  $a$  is the acceleration and  $t$  is the time for the ion to traverse the sheath. The acceleration is given by

$$a = \frac{eE}{m} = \frac{eV_f}{\lambda_D m}. \quad \{89\}$$

Given that the surface is at  $x=0$ , then the time,  $t$ , is

$$t = \sqrt{\frac{2\lambda_D}{a}}. \quad \{90\}$$

The maximum kinetic energy provided per ion is then

$$\begin{aligned} KE &= eV_f \\ &= \frac{1}{2} kT_e \ln\left(\frac{M}{2\pi m}\right). \end{aligned} \quad \{91\}$$

For an electron temperature of 18 eV, as given by Schwirzke [Ref. 4], the kinetic energy of copper ions is

$$KE = 88.4 \text{ eV/ion.} \quad \{92\}$$

The fraction of the required cohesive energy which is provided by the maximum kinetic energy of the ions is then

$$\frac{N_i KE_i}{N_n E_c} = 0.557. \quad \{93\}$$

$N_i/N_n$  is the ratio between the numbers of ions and neutrals as found in the previous section (0.022). This estimates a significant contribution.

Ions will be produced throughout the sheath, thus the actual contribution of their kinetic energy will be less than that given above. First it will be assumed that the ions are produced in a linear fashion such that one ion will be produced over each interval  $\lambda_D/N_i$ , where  $N_i$  represents the total number of ions produced. It is also assumed that

the potential increases linearly with distance from the surface. The kinetic energy contribution from the ion produced in the  $j$ th interval from the surface is then

$$KE_j = KE_{\max} \frac{j}{N_i} \quad \{94\}$$

The total kinetic energy contribution from all of the ions is then

$$KE_{tot} = \frac{KE_{\max}}{N_i} \sum_{j=1}^{N_i} j \quad \{95\}$$

If  $f(x) = j$ , then

$$\int_j^{j+1} f(x) dx \geq j \quad \{96\}$$

so that

$$\sum_{j=1}^{N_i} \int_j^{j+1} f(x) dx = \int_1^{N_i} f(x) dx \geq \sum_{j=1}^{N_i} j \quad \{97\}$$

The upper bound on the total kinetic energy is then

$$\begin{aligned} KE_{tot} &= \frac{KE_{\max}}{N_i} \int_1^{N_i} f(x) dx \\ &= \frac{1}{2} N_i KE_{\max} - \frac{1}{2N_i} KE_{\max} \end{aligned} \quad \{98\}$$

In the limit as  $N_i$  becomes large the average kinetic energy contribution per ion becomes

$$KE_{ion} = \frac{KE_{tot}}{N_i} = \frac{1}{2} KE_{\max} \quad \{99\}$$

Thus the ion's kinetic energy provides approximately 27.9% of the total energy required for vaporization.

## APPENDIX C. DETAILED CALCULATION OF THE SHEAR STRESS

Whenever there is a viscous fluid moving with a nonuniform velocity shear stresses will be present. These stresses can be considered to act as if there is a frictional force between the elements of the fluid. This force coming from the 'friction' generated between adjacent elements moving at different velocities. Figure A-1 shows the viscous stress components in the spherical coordinate system  $(r, \theta, \phi)$ . These components, as derived by Lancaster [Ref. 15, p.85], are

$$\begin{aligned}
 p_{rr} &= -p + 2\eta \frac{\partial v_r}{\partial r} \\
 p_{\theta\theta} &= -p + 2\frac{\eta}{r} \left( \frac{\partial v_\theta}{\partial \theta} + v_r \right) \\
 p_{\phi\phi} &= -p + \frac{2\eta}{r \sin \theta} \left( \frac{\partial v_\phi}{\partial \phi} + v_r \sin \theta + v_\theta \cos \theta \right) \\
 p_{r\theta} &= p_{\theta r} = \eta \left[ r \frac{\partial}{\partial r} \left( \frac{v_\theta}{r} \right) + \frac{1}{r} \frac{\partial v_r}{\partial \theta} \right] \\
 p_{\theta\phi} &= p_{\phi\theta} = \eta \frac{1}{r} \left[ \frac{\partial v_\phi}{\partial \theta} + \frac{1}{r \sin \theta} \frac{\partial v_\theta}{\partial \phi} - \frac{v_\phi \cot \theta}{r} \right] \\
 p_{r\phi} &= p_{\phi r} = \eta \left[ r \frac{\partial}{\partial r} \left( \frac{v_\phi}{r} \right) + \frac{1}{r \sin \theta} \frac{\partial v_r}{\partial \phi} \right]
 \end{aligned}$$

On a planar surface defined by  $\theta = \pi/2$  the stress which acts to counter the surface tension is  $p_{r\theta}$ . The purpose of this appendix is to calculate this stress component.

Equation (56) gives the stream function to be

$$\Psi(r, \lambda) = \frac{\mu_o l^2 r}{4\pi^2 \eta} [a\lambda^2 + b\lambda + c + (1+\lambda) \ln(1+\lambda)] \quad (56)$$

where  $\lambda = \cos \theta$ . The first boundary condition

$$\Psi(r, 0) = 0 \quad (57)$$

implies that  $c=0$ . In order to calculate the shear stress the velocities in the radial and theta directions are required, these are provided by the stream function as follows:

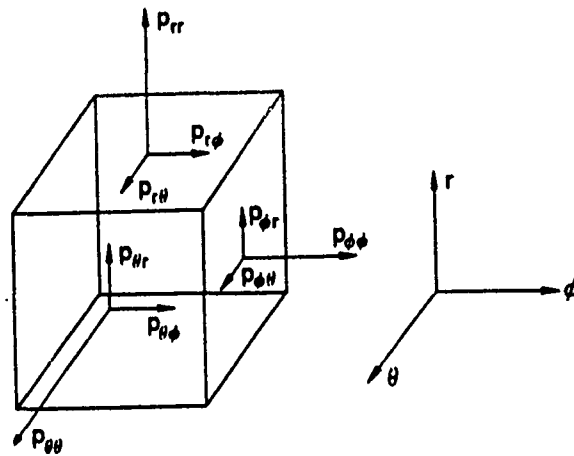


Figure 63. Components of viscous in the spherical coordinate system. [Ref. 15, p.85]

$$\begin{aligned}
 v_r &= \frac{1}{r^2 \sin \theta} \frac{\partial \Psi}{\partial \theta} \\
 &= -\frac{1}{r^2} \frac{\partial \Psi}{\partial \lambda} \\
 &= \frac{\mu_0 I^2}{4\pi^2 \eta} \frac{1}{r} [2a\lambda + b + \ln(1+\lambda) + 1]
 \end{aligned}
 \tag{103}$$

$$\begin{aligned}
 v_\theta &= -\frac{1}{r \sin \theta} \frac{\partial \Psi}{\partial r} \\
 &= -\frac{1}{r \sqrt{1-\lambda^2}} \frac{\partial \Psi}{\partial r} \\
 &= -\frac{\mu_0 I^2}{4\pi^2 \eta} \frac{1}{r \sqrt{1-\lambda^2}} [a\lambda^2 + b\lambda + (1+\lambda) \ln(1+\lambda)]
 \end{aligned}
 \tag{104}$$

The required partial derivatives are

$$\begin{aligned}
\frac{\partial v_r}{\partial \theta} &= \frac{\partial v_r}{\partial \lambda} \frac{d\lambda}{d\theta} \\
&= -\sqrt{1-\lambda^2} \frac{\partial v_r}{\partial \lambda} \\
&= \sqrt{1-\lambda^2} \frac{\mu_o I^2}{4\pi^2 \eta} \frac{1}{r} \left[ 2a + \frac{1}{1+\lambda} \right]
\end{aligned}
\tag{105}$$

and

$$\frac{\partial}{\partial r} \left( \frac{v_\theta}{r} \right) = \frac{\mu_o I^2}{4\pi^2 \eta} \frac{1}{\sqrt{1-\lambda^2}} \frac{2}{r^3} [a\lambda^2 + b\lambda + (1+\lambda) \ln(1+\lambda)]
\tag{106}$$

Placing these equations into the equation for the shear stress yields

$$\begin{aligned}
p_{r\theta} &= \frac{\mu_o I^2}{4\pi^2 r^2} \frac{2}{\sqrt{1-\lambda^2}} [a\lambda^2 + b\lambda + (1+\lambda) \ln(1+\lambda)] + \frac{\mu_o I^2}{4\pi^2 r^2} \sqrt{1-\lambda^2} \left[ 2a + \frac{1}{1+\lambda} \right] \\
&= \frac{\mu_o I^2}{4\pi^2 r^2} \left\{ \frac{2}{\sqrt{1-\lambda^2}} [a\lambda^2 + b\lambda + (1+\lambda) \ln(1+\lambda)] + \sqrt{1-\lambda^2} \left( 2a + \frac{1}{1+\lambda} \right) \right\}.
\end{aligned}
\tag{107}$$

## LIST OF REFERENCES

1. Chen, F.F., *Introduction to Plasma Physics and Controlled Fusion*, 2d ed., v. 2, Plenum Press, 1984.
2. Robson, A.E. and Thonemann, P.C., "An Arc Maintained on an Isolated Metal Plate Exposed to a Plasma," *Proceedings of the Physical Society*, v. 73, pp.508-512, March 1959.
3. Schwirzke, F. and Taylor, R.J., "Surface Damage by Sheath Effects and Unipolar Arcs," *Journal of Nuclear Materials*, v. 93 & 94, pp.780-784, 1980.
4. Schwirzke, F., "Unipolar Arc Model," *Journal of Nuclear Materials*, v. 128 & 129, pp.609-612, 1984.
5. Maissel, L.I. and Francombe, M.H., *An Introduction to Thin Films*, Gordon and Breach Science Publishers, 1973.
6. Eckterova, L., *Physics of Thin Films*, Plenum Press, 1977.
7. SLOAN Technology Corp., *Handbook of Thin Film Materials*.
8. Vacuum-Electronics Corp., "401" Series Evaporator and Pumping Stations Models VE-401, VS-401, and VP-401 Operation and Maintenance Manual.
9. SLOAN Technology Corp., *Deposit Thickness Monitor DTM-2a Installation and Operating Manual*.
10. Weston, R.L., "CO2 Pulsed Laser Damage Mechanism and Plasma Effects (Focused Beam)," Master's Thesis, Naval Postgraduate School, Monterey, California, December 1986.

11. Wojtowich, A.R., "Background Gas Pressure Dependence of Unipolar Arcing on Soda Lime Glass and Plastic Induced by a CO<sub>2</sub> Pulsed Laser," Master's Thesis, Naval Postgraduate School, Monterey, California, June 1988.
12. Henson, M.V., "Generation of Electromagnetic Radiation Due to Laser Induced Breakdown and Unipolar Arcing," Master's Thesis, Naval Postgraduate School, Monterey, California, September 1989.
13. Cambridge Instruments Limited TL 2025-OM, *Stereoscan 500 Scanning Electron Microscope Operating Instructions*, Issue 3, April 1985.
14. Wieckert, C., "Plasma Induced Arcs," *Journal of Nuclear Materials*, 76 & 77, pp.499-502, 1978.
15. *The Physics of Welding*, 2nd ed., Pergamon Press, 1986.
16. Croxton, C.A., *Statistical Mechanics of the Liquid Surface*, John Wiley & Sons, 1980.
17. Andrews, J.G. and Atthey, D.R., "Hydrodynamic limit to penetration of a material by a high power beam," *Journal of Physics D: Applied Physics*, v.9, pp.2181-2194, 1976.
18. Naval Postgraduate School Report NPS-61-84-004, *Short Pulse Laser and Plasma Surface Interactions*, by F. Schwirzke, 2 April 1984.
19. Lundquist, S., "On the hydromagnetic viscous flow generated by a diverging electric current," *ARKIV FOR FYSIC*, v.40, no.5, pp.89-94, 8 January 1969.
20. Matsunawa, A., "Role of Surface Tension in Fusion Welding (Part 3)," *Trans JWRI*, Osaka University, v. 13, no. 1, pp.147-156, 1984.
21. White, F.M., *Fluid Mechanics*, 2d ed., McGraw-Hill Book Company, 1986.

22. Kittel, C., *Introduction to Solid State Physics*, 6th ed., John Wiley & Sons, Inc., 1986.

## INITIAL DISTRIBUTION LIST

	No. Copies
1. Defense Technical Information Center Cameron Station Alexandria, VA 22304-6145	2
2. Library, Code 0142 Naval Postgraduate School Monterey, CA 93943-5002	2
3. Professor Fred R. Schwirzke Code 61Sw Naval Postgraduate School Monterey, CA 93943	2
4. Professor Richard C. Olsen Code 61Os Naval Postgraduate School Monterey, CA 93943	2
5. Chairman Karlheinz E. Woehler Code 61Wh Naval Postgraduate School Monterey, CA 93943	2
6. LT Richard K. Downs Department Head Class 112 Surface Warfare Officers School Command Newport, RI 02841-5012	2